**NTNU – Trondheim**
Norwegian University of
Science and Technology

# Electrohydrodynamic Structuring of Colloidal Particles on Leaky Dielectric Drops

Julie Janine Ravnanger
Seth

Master of Science in Physics and Mathematics
Submission date: September 2013
Supervisor: Jon Otto Fossum, IFY
Co-supervisor: Marcio Carvalho, PUC-Rio

Norwegian University of Science and Technology
Department of Physics

**Abstract**

This Master's thesis shows experimentally how colloidal particles in leaky dielectric drops are actively structured by applying a DC electric field. Colloidal particles dispersed in small droplets with a diameter of 0.1 mm show similar structuring to what has previously been observed on bigger drops (1 mm), such as ribbon formation, spinning domains and pupil effects. It is shown how electrohydrodynamic assembly of colloidal particles on a drop surface depends on the electric field strength, and how this enables fast assembly of the particles. The particles used in the experiments are clay particles, layered double hydroxides and insulating beads. The layered double hydroxides show similar structuring to the clay particles. The results suggest that active control of colloidal particles on leaky dielectric drops by an electric field can lead to new ways of producing Janus shells and other 'smart armoured' droplets.

**Sammendrag**

Denne masteravhandlingen beskriver et eksperimentelt arbeid som omhandler hvordan partikler suspendert i svakt elektrisk ledende dielektriske dråper, kan struktureres ved hjelp av et påtrykt elektrisk felt. Det beskrives hvordan kolloidpartikler i små dråper med en diameter 0.1 mm viser lignende strukturering som det som har blitt observert tidligere på større dråper (ca. 1 mm). Partiklene ordner seg i bånd, i spinnende domener, og i pupille lignenede strukturer. Det demonstreres at elektrohydrodynamisk aggregering av kolloidiale partikler på en dråpeoverflate avhenger av den elektriske feltstyrken, og at dette muliggjør en rask aggregering av partiklene. Partikler brukt i eksperimentene er leirepartikler, lagdelte hydroksider og ikke-ledende partikler. Lagdelte hydroksider viser lignende strukturering som leirepartikler. Resultatene antyder at aktiv kontrollering av kolloidpartikler på slike dielektriske dråper kan lede til nye metoder for produksjon av Janus-skall og andre 'smarte innkapslede' dråper.

# Contents

# Preface

The work presented in this Master's thesis is done in my final semester of studies for the degree MSc in Applied Physics and Mathematics at the Norwegian University of Science and Technology (NTNU). The research has been carried out for the Complex Systems and Soft Materials group at the Department of Physics at NTNU, but all the experiments were performed at the Laboratory of Micro-Hydrodynamics and Porous Media (LMMP) at Pontifícia Universidade Católica do Rio de Janeiro (PUC-Rio) in Brazil.

First, I would like to thank my supervisor, Professor Jon Otto Fossum, for giving me the opportunity to work in his group and for all the guidance he provided during the semester. I am also very grateful for getting the opportunity to stay one semester at PUC-Rio.

I would like to thank my co-supervisor, Professor Marcio Carvalho at PUC-Rio, for letting me work in his laboratory and for being so welcoming and helpful. I would also like to thank the rest of the LMMP group for including me, and especially Felicle Lopez, the laboratory manager, for always helping with technical problems.

Postdoc Zbigniew Rozynek has thought me a lot about droplet systems and I am very thankful for all the advice and inspiration he has given, and for always answering my questions. I would also like to thank PhD student Alexander Mikkelsen for helping me with the experiments and Master student Emilie Lund Johnsrud for the work we did together on droplet production.

Trondheim, 09.09.2013 Janine Ravnanger Seth

# Chapter 1

# Introduction

This Master thesis presents results of a study done on colloidal particles dispersed in oil-in-oil emulsion drops in an electric field. Many experiments were done with droplets made in co-flowing microfluidic channels.

When an electric field is applied to a liquid, fluid flow can be induced. An electric field applied to oil-in-oil emulsion drops will induce electrohydrodynamic (EHD) flow, described by Taylor's leaky dielectric model [7]. This system has been extensively studied, and the drops have shown different responses to electric fields, such as deformation, break-up, rotation and coalescence [6, 11, 13].

Colloidal particles will bind strongly to a liquid-liquid interface. This has been used to stabilize surfactant free emulsions, known as Pickering emulsions [27]. The particles will work as a mechanical barrier preventing coalescence and destabilization of the emulsion. These emulsions have been used in various food and cosmetics products [28]. They have also attracted interest as templates for functional composite materials, such as colloidosomes. Colloidosomes are hollow elastic shells consisting of colloidal particles and can be fabricated by the self-assembly of colloidal particles onto the interface of emulsion droplets [29]. The permeability and elasticity is of colloidosomes can be controlled. They have a wide range in applications, with one possible being drug delivery [30].

Dommersnes et al. [3] recently published a paper where they reported how an electric field can be used to structure and dynamically control colloidal

particles on oil-in-oil emulsion drops, due to EHD and electrorheological effects. The behaviour of the particles is well understood, but some aspects, for instant the influence of sedimentation on the particles needs further study. More about structuring of colloidal particles on liquid drops can be found in section 2.5.

The motivation for this thesis was to continue the study of particle formations on leaky dielectric liquid drops, starting by down-scaling experiments done by Dommersnes et al. to droplets in the size $\sim 100\,\mu\text{m}$. The thesis starts with some relevant background theory and models in chapter 2. Then the experimental procedure and setup is explained in chapter 3, before the results are presented and discussed in chapter 4. First, the results from experiments done with the droplets produced in microfluidic co-flowing channels are presented. Then, results from experiments done with insulating beads on bigger drops made with a pipette are discussed, and lastly results from experiments done with layered double hydroxides on drops is included. Finally, a conclusion is presented in chapter 5, together with suggestions for future studies.

# Chapter 2

# Theory

This chapter gives an overview of theoretical background relevant to this thesis. Some models leading up to Taylor's leaky dielectric model are presented, as well as theory on electrocoalescence and Janus particles. Droplet production in microfluidic channels is discussed, and finally, some theory of the materials used, clay and layered double hydroxides is included.

## 2.1 Dielectric sphere in uniform field

To understand how drops are influenced by an electric field it is useful to start looking at what happens when a linear dielectric solid sphere is placed in a uniform electric field $\mathbf{E_0}$. The problem is solved using Maxwell's equations given in [4] and the boundary conditions

$$\left.\begin{aligned} V_{in} &= V_{out} && \text{at } r = R \\ \epsilon\frac{\partial V_{in}}{\partial r} &= \epsilon_0\frac{\partial V_{out}}{\partial r} && \text{at } r = R \\ V_{out} &\to -E_0 r\cos\theta && \text{at } r \gg R \end{aligned}\right\} \tag{2.1}$$

where $V_{in}$ and $V_{out}$ is the potential inside and outside of the sphere. The electric field is the gradient of this scalar potential

$$\boldsymbol{E} = -\nabla V. \tag{2.2}$$

Using Laplace's equation

$$\nabla^2 V = 0 \tag{2.3}$$

and separation of variables one finds the potential inside the sphere

$$V_{in}(r,\theta) = -\frac{3E_0}{\epsilon_r + 2}, \tag{2.4}$$

and the potential outside the sphere

$$V_{out}(r,\theta) = \left(\frac{\epsilon_r - 1}{\epsilon_r + 2}\right)\frac{R^3}{r^2}E_0\cos\theta - rE_0\cos\theta, \tag{2.5}$$

where $\epsilon_r = \epsilon_{in}/\epsilon_{out}$. The first term in equation (2.5) is the potential from the induced dipole. Then, by solving equation (2.2), one finds that the field inside the sphere is uniform, and given by

$$\boldsymbol{E_{in}} = \frac{3}{\epsilon_r + 2}\boldsymbol{E_0} \tag{2.6}$$

A schematic of the electrical field is shown in figure 2.1. The potential from a general dipole field is given by

$$V = \frac{p\cos\theta}{4\pi\epsilon_0 r^2}, \tag{2.7}$$

where $p$ is the magnitude of the *dipole moment*. Using this and equation (2.5) one finds that

$$\boldsymbol{p} = 4\pi\epsilon_0\frac{\epsilon_r - 1}{\epsilon_r + 2}R^3\boldsymbol{E_0} \tag{2.8}$$

Since the total dipole is the volume integral of the polarization, $\boldsymbol{P}$, the polarization is given by

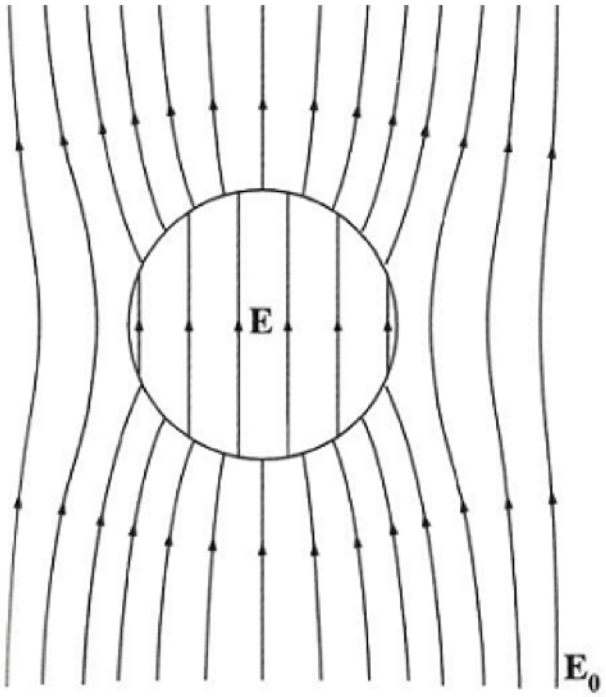


Figure 2.1: Field lines in and around a dielectric solid sphere in a uniform electric field. Figure adapted from [4].

$$\boldsymbol{P} = \frac{p}{\frac{4}{3}\pi R^3} = 3\epsilon_0 \frac{\epsilon_r - 1}{\epsilon_r + 2} \boldsymbol{E_0}, \tag{2.9}$$

and is parallel to the electric field. The polarization charge on the surface of the sphere becomes

$$q_\sigma = \boldsymbol{P} \cdot \hat{n} = P \cos\theta, \tag{2.10}$$

which shows that on one pole we get positive surface charges and on the other pole we get negative surface charges. Hence, a dielectric sphere in a uniform electric field becomes a dipole.

A detailed derivation of equation (2.4) and (2.5) is found in Appendix A.

## 2.2 The perfect dielectric model

For dielectric drops immersed in a dielectric fluid an applied uniform electric field will cause the drops to have a spheroidal form. O'Konski and Thatcher [5] found in a study in 1953 drops in a dielectric fluid to have a prolate form when an electric field was applied.

By maximizing the free surface energy and the electrostatic free energy, the only contributions to free energy which depend on the deformation, they found that the deformation of conducting drops in a dielectric media is given by

$$D = \frac{9}{16}\frac{E^2\epsilon_1 a}{\gamma}, \tag{2.11}$$

where $E$ is the applied field strength, $\varepsilon_{out}$ is the relative permittivity of the dielectric media, $\varepsilon_0$ is the vacuum permittivity, $a$ is the droplet radius and $\gamma$ is the interfacial tension. The equation is only valid for small pertubations. Allan and Mason [6] found the identical result from balancing the electrical and interfacial tension.

The deformation in equation (2.11) is defined as [8]

$$D = \frac{d_\perp - d_\parallel}{d_\perp + d_\parallel} \tag{2.12}$$

where $d_\perp$ and $d_\parallel$ are the axis of the spheroid perpendicular and parallel to the applied electric field. The deformation $D$ is positive for prolate deformation and negative for oblate deformation. For a conducting droplet in equilibrium the pressure inside and outside the drop is uniform thus the electric stresses on the droplet surface are balanced by the interfacial tension. The sphere will induce a dipole that varies as $\cos\theta$, $\theta$ being the angle from the electric field, and a field normal to the surface creates a stress that varies as $\cos^2\theta$. The droplet will be stretched in the direction of the applied field and will get a prolate deformation.

Allan and Mason also found that for dielectric droplets in dielectric media the deformation is

$$D = \frac{9}{16}\frac{E^2\epsilon_1 r}{\gamma}\frac{(\epsilon_1 - \epsilon_2)^2}{(\epsilon_2 - 2\epsilon_1)^2} \tag{2.13}$$

The charges will in this case vary over the surface as was found in equation (2.10). The charges at the poles will be stretched by the applied field in opposite directions giving the sphere a prolate deformation.

Even though prolate deformation was predicted in both cases, Allan and Mason also observed oblate deformations in some cases. This led Taylor (1966) to believing that the surrounding fluid could not be a perfect dielectric liquid, and thus to the development of the leaky dielectric model.

## 2.3 Taylor's leaky dielectric model

Taylor [7] believed that real dielectric liquids would conduct a small amount of electrical current, and thus could not be viewed as perfect dielectrics. Because of this there will exist a tangential stress on the drop that cannot be balanced by surface tension or a constant external or internal pressure. Thus, it will be impossible for a drop to maintain a spherical form when an electric field is applied, and for this to happen there has to be some pressure difference between the inside and outside of the drop. This pressure difference has to come from fluid flows on the inside and outside of the drop.

Taylor assumed that the potentials could be approximated of the same as with a static conducting sphere in a conducting fluid. To assume that the potential will be the same as for a static sphere will not be correct when currents that convect charge exist, but in most cases this effect will be small. The potentials outside and inside of the sphere will then be

$$V_{out} = E_0 \cos\theta \left( r + \frac{1-R}{2+R} \frac{a^3}{r^2} \right), \tag{2.14}$$

$$V_{in} = \frac{3E_0 r \cos\theta}{2+R} \tag{2.15}$$

where $R$ is the ratio of the electrical conductivity of the sphere and the outer conductor, $R = \sigma_{in}/\sigma_{out}$, and $a$ is the radius of the sphere.

Taylor found the deformation of the spheroid, given weak electric fields and thus small deformation, to be

$$D = \frac{9}{16} \frac{a\epsilon_{out}\epsilon_0 E_0^2}{\gamma S(2+R)^2} \left[ S(R^2+1) - 2 + 3(RS-1) \left( \frac{2\lambda+3}{5\lambda+5} \right) \right], \tag{2.16}$$

where $\gamma$ is the surface tension. $S = \frac{\varepsilon_{out}}{\varepsilon_{in}}$ and $\lambda = \frac{\mu_{in}}{\mu_{out}}$, where $\varepsilon$ is the permittivity and $\mu$ is the viscosity [8].

As can be seen from equation (2.16) the direction or the strength of the electric field does not influence if the deformation is prolate or oblate, only the parameters $S$, $R$ and $M$ do. Taylor introduced the discriminating function

$$\phi(S, R, M) = S(R^2 + 1) - 2 + 3(RS - 1)\left(\frac{3M + 2}{5M + 5}\right) \tag{2.17}$$

that decides is the deformation is prolate or oblate. If $\phi(S, R, M)$ is positive the drop will be prolate, and if $\phi$ is negative the drop will be oblate.

Taylor also found the electrohydrodynamic flow velocity at the drop boundary to be

$$v_\theta = -\frac{9}{8\pi}\frac{a\varepsilon_{out}\varepsilon_0 E^2}{(2 + R)^2}\frac{RS - 1}{5(\mu_{in} + \mu_{out})}\sin(2\theta), \tag{2.18}$$

where $\theta$ is the polar angle. From equation (2.18) we can see that the direction of the circulation depends on the parameter $RS$. When $RS < 1$ the circulation is directed from pole to equator at the interface, and for $RS > 1$ it will be directed from equator to the pole. Figure 2.2 (a) and (b) shows the streamlines for both cases, the direction of the flow indicated by arrows.

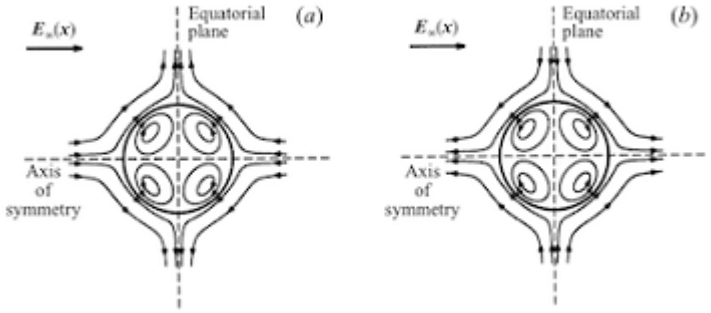


Figure 2.2: Qualitative circulation patterns according to the leaky dielectric model. (a) $RS < 1$ (b) $RS > 1$. Figure adapted from [13].

$RS$ characterizes the conduction response of the fluids. The product can be defined as [8]

$$SR = \frac{t_{c,out}}{t_{c,in}}, \text{ where } t_{c,in} = \frac{\epsilon_{in}}{\sigma_{in}} \text{ and } t_{c,out} = \frac{\epsilon_{out}}{\sigma_{out}} \tag{2.19}$$

where $t_c$ is the charge relaxation time, a measure of how fast the charges are supplied to restore equilibrium. If $RS > 1$ ($t_{c,out} > t_{c,in}$) the conductivity is

larger in the fluid around the drop, than in the drop itself. Thus, the charges inside the drop will align with the field faster than outside, and the interface will be dominated by charges from the droplet. The dipole moment will in this case be aligned parallel to the applied electric field, and because the charges are attracted by the charges on the electrodes the drop will be pulled in a prolate shape. For the opposite case, where $RS < 1$ ($t_{c,out} < t_{c,in}$) the conductivity in the surrounding fluid is higher, and the dipole moment of the drop is aligned antiparallel with the applied electric field. In this case the drop can be either oblate or prolate, depending on the viscosities of the two fluids. In Figure 2.3 the deformation is shown for three different viscosity ratios $\lambda$.

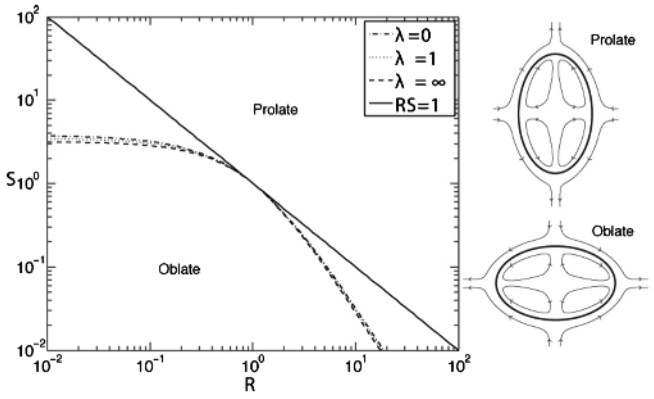


Figure 2.3: $RS$ diagram of oblate and prolate deformation for three different viscosity ratios, $\lambda$, determined by Taylor's discriminating function. Figure adapted from [8].

## 2.4 Coalescence of droplets induced by an electric field

For leaky dielectric drops there are two effects mainly deciding how two drops will interact, the dielectrophoretic effect and the EHD interactions. The dielectrophoretic motion will always be attractive if the drops are aligned in the direction of the field, and the velocity scales as $O(a/h)^4$, where $a$ is the radius of the drops and $h$ the center-to-center distance. The velocity from the EHD driven movement scales as $O(a/h)^2$, and this relative motion can either be attractive or repulsive. Since the velocity from the EHD force scales as $O(a/h)^2$, and the velocity from the dielectrophoretic motion scales as $O(a/h)^4$, the EHD force is dominant at long distances and the electrophoretic forces at short distances. In the case that the interfacial tension is low, there is also an deformation-induced contact characteristic at small separation distances that influences the way the drops interact [13].

What decides whether the relative motion from the EHD interaction is attractive or repulsive is the conductivity and resistivity of the two fluids. If $RS < 1$, the flow around the drops will make them move towards each other, and if $RS > 1$ the flow will cause the drops to move apart.

Baygents et al. [13] studied the movement of two drops of equal size in axisymmetric geometry numerically in 1998. They observed three classes of behaviours, given sufficiently large capillary number and large enough $h/a$. These three different cases are shown in Figure 4.6. In (a) the drops deforms oblately and then they coalesce, in (b) they deform prolately and then they coalesce and in (c) they deform prolately and then they move apart.

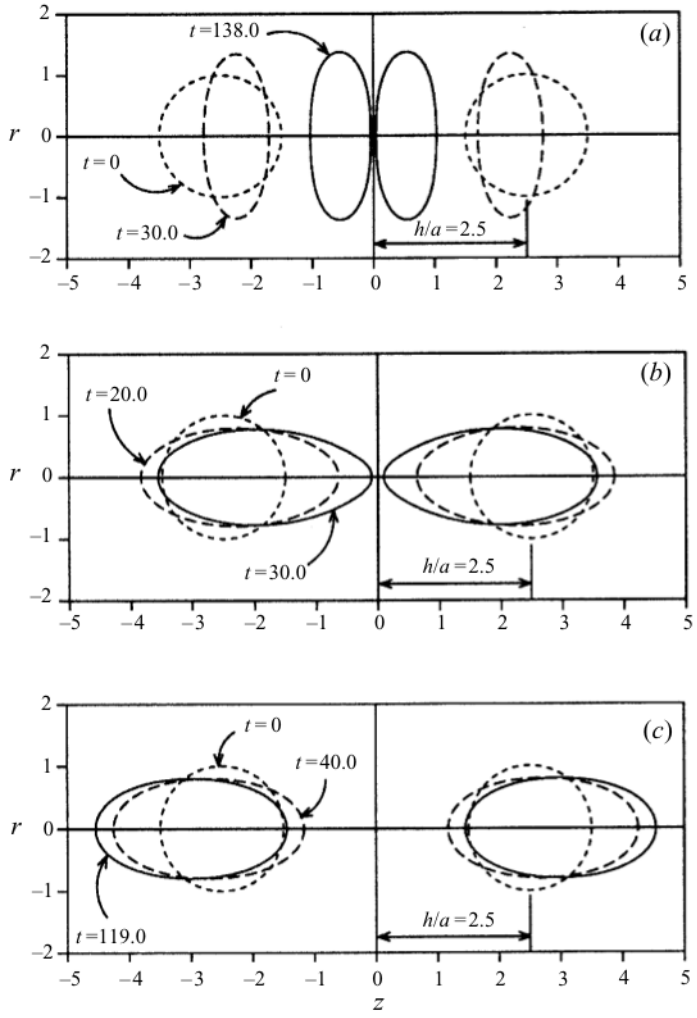


Figure 2.4: Characteristic behaviours of drop deformation and interaction in the leaky dielectric model. (a) $RS < 1$. Drops deform oblately and come together. (b) $RS < 1$. Drops deform prolately and come together. (c) $RS > 1$. Drops deform prolately and move apart. Figure adapted from [13].

## 2.5 Structuring of colloidal particles on liquid drops

Structuring of colloidal particles on leaky dielectic drops by applying electric fields has been studied by Dommersnes et al. [3]. Clay particles were dispersed throughout a silicone drop immersed in castor oil, and an equatorial clay ribbon was observed when a DC electric field was applied, shown in Figure 2.5.

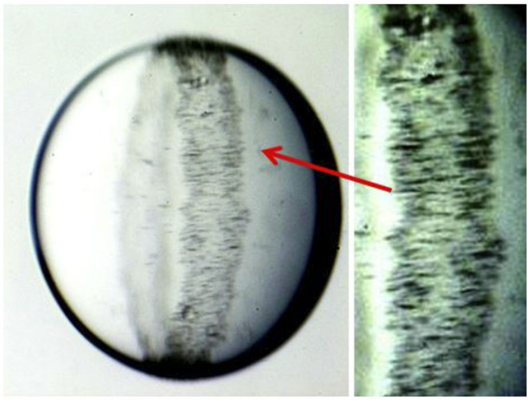

Figure 2.5: Silicone oil drop with clay ribbon in an applied field of 200 V/mm. 2D dipolar chain formations of clay particles can be seen in the ribbon. The drop radius is about 1 mm. Figure adapted from [3].

They observed that the width of the ribbon increases with increased clay concentration and for concentrations above 0.5% it increases with increased field strength. That the width of the ribbon increases when the electric field strength is increased is contrary to what one would expect if the only working mechanism is the EHD flow. When the electric field is increased the particle dipole-dipole interactions start playing important role and begin to compete against the EDH effect. When both the clay concentration and electric field strength are high enough, the dipole-dipole interactions will be dominant in the system, and this will lead to significant suppressing of the EDH flow. The dipole-dipole interactions will cause the clay particles to align in chain-like structures (further discussed in section 2.8.1). On the drops, the chains grow from the ribbon towards each pole. The higher the electric field strength is, the longer the chains will be, but the length will naturally be limited by

the clay concentration located in the ribbon. Once the chains are growing they effectively increase the conductivity on the drop surface, since clay is more conductive than both oils. This will suppresses the EHD flow because it prevents a charge build-up on the drop surface.

The electrohydrodynamic (EDH) flow explains stability of the ribbon once it has been formed, but it does not explain why the particles migrate to the surface. If the particles follow the EHD streamlines they will approach the surface, but will turn before they are absorbed. Therefore it has to be some other mechanism making them go to the surface. Dommersnes et.al. suggests that this could come from attraction to clay particles already on the surface, because of the dipole-dipole interaction between the particles. They also suggest that it could come from charge uptake on the clay particles which would make them move in the electric field. In addition particle sedimentation could play an important role in getting the particles from the bulk to the surface of the drops.

Because the width of the ribbon could be controlled by the electric field strength Dommersnes et al. did experiments where they varied between two different field strengths, where one of the field strengths would make a thin ribbon and the other one would make the clay cover the drop. Varying between these two fields would make a pattern that seems like an eye pupil. This effect was found using four different clay samples, and has to be related to the fact that the clay is more conductive than both oils, and thus will modify the electric field. For insulating beads and metallic-coated particles this effect was not observed, the insulating beads only formed an equatorial ribbon, and the metallic-coated beads only formed chain-like structures on the surface, as shown in Figure 2.6.

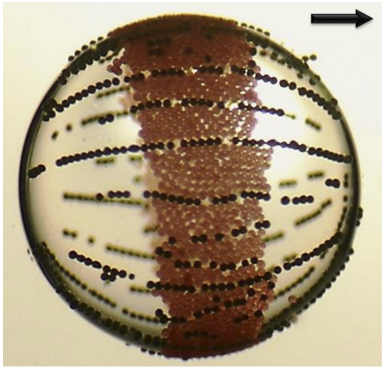

Figure 2.6: Silicone oil drop covered with insulating PE beads and metallic-coated beads in applied field of strength 250 V/mm. The insulating beads form an equatorial ribbon, while the metallic-coated particles form chain-like structures. The drop radius is about 1 mm. Figure adapted from [3].

## 2.6 Janus particles

The name Janus particles was first introduced by P. G. de Gennes in his Nobel Prize address. He borrowed the name from the Roman God, Janus, who had two faces looking into opposite directions [31], and the name is now used to describe particles that have different properties on opposing sides.

Janus particles have many potential applications. Some industrial applications can be as amphiphilic surfactants used to stabilize oil/water emulsions, electronic paper and displays, catalysis and for making water-repellent textiles [33]. They can also be used in biomedical applications, such as drug delivery, molecular imaging and bimolecular labeling [32].

The preparation of Janus particles is a key point for extending their use. Different techniques have been used, but they all have advantages and limitations, and if the techniques are to be used in industrial applications it is important that they are low-cost techniques that allows for high production. There exists some different preparation strategies, such as self-assembly of the components, masking or phase separation [34].

Colloidosomes are hollow elastic shells consisting of colloidal particles, and these can be fabricated by the self-assembly of colloidal particles onto the interface of emulsion droplets [29]. The permeability and elasticity of colloidosomes can be controlled. They have a wide range in applications, with one possible being drug delivery [30].

Janus colloidal shells are a new class of patchy structures combining Janus particles and colloidosomes. These shells have so far only been produced using a flow-focusing microfluidic setup [35].

## 2.7 Production of droplets in microfluidic channels

There are three main ways of producing droplets in microfluidic channels: (1) production in concentric flow cell (Figure 2.7), (2) production in a T-juction (Figure 2.8) and (3) production in a flow-focusing device (Figure 2.9). In all these different geometries both the dispersed phase and the continuous phase are driven independently into the microchannel. The size of the droplets will depend on the geometry of the channels, flow rates, interfacial tension and the viscosities of the fluids. The size will be determined by the pressure from the external flow and viscous shear stresses competing against the capillary pressure that resists the deformation [14].

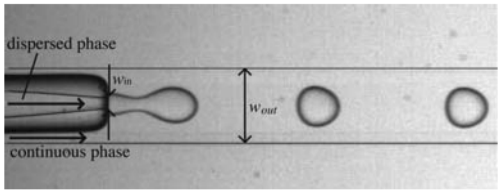


Figure 2.7: Production of droplets in co-flowing channels. Figure adapted from [14].

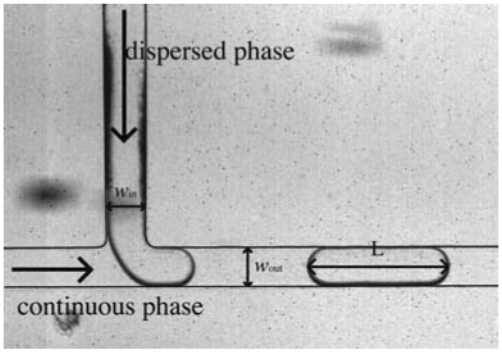


Figure 2.8: Production of droplets in a t-junction. Figure adapted from [14].

Cramer et al. [15] showed that for co-flowing streams the breakup of the liquid streams into droplets could be separated into two different regimes;

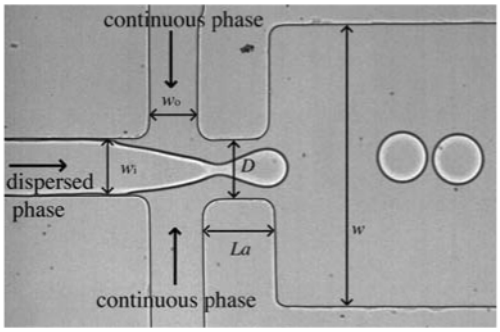


Figure 2.9: Production of droplets in a flow-flocusing device. Figure adapted from [14].

dripping and jetting. In the dripping regime, the drops pinch off near the inner tube's tip and in jetting the droplets pinch off from a thread downstream from the tube tip. The drop production in the dripping regime will appear at lower flow rates of both the dispersed and continuous phase. It creates bigger droplets than in the jetting mode, but is more stable and the appearance of satellite droplets is much smaller. The effects of flow rates, viscosities and interfacial tension in concentric flow cells are discussed further in Appendix B.

## 2.8 Clay minerals

Clays minerals are materials based on a two-dimensional stack of inorganic layers, and they can be natural or synthetic. The individual layers are made of elemental sheets that can be *tetrahedral* or *octahedral*. The tetrahedral sheet is typically made of $SiO_4^{4-}$ or $AlO_4^{5-}$ tetrahedra forming a two-dimensional hexagonal mesh pattern. The octahedral sheet is made up of octahedra linked together by shearing edges [17]. The difference between these sheets is shown in Figure 2.10.

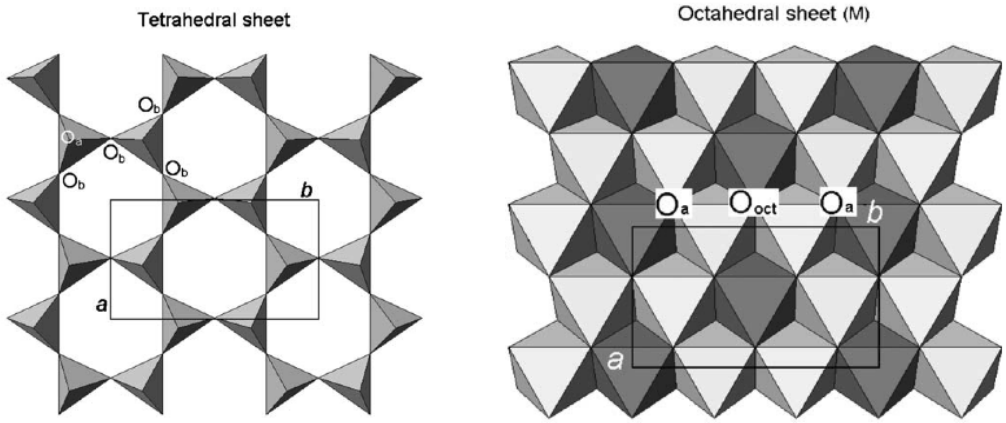


Figure 2.10: The tetrahedral and octahedral sheet. Figure adapted from [18].

Clay minerals can be divided into two groups depending on the combination of the tetrahedral and the octahedral sheets. If one tetrahedral sheet is bonded to one octahedral sheet it is called a 1:1 layered structure, and if the octahedral sheet is between two tetrahedral sheets it is called a 2:1 layered structure. The 1:1 and 2:1 layer is shown in Figure 2.11.

In the octrahedral sheet there will be a negative surface charge on the layers, balanced by exchangeable cations. Because of these, the layers can stack up, forming clay particles consisting of up to several hundred layers. In between these layers there will be an *interlayer distance* and in some clays molecules can be intercalated here, a phenomenon called *swelling*. Both crystalline swelling and macroscopic swelling can occur. In crystalline swelling a limited number of molecules are intercalated and with water as intercalant the process is reversible. In macroscopic swelling or exfoliation there are so many

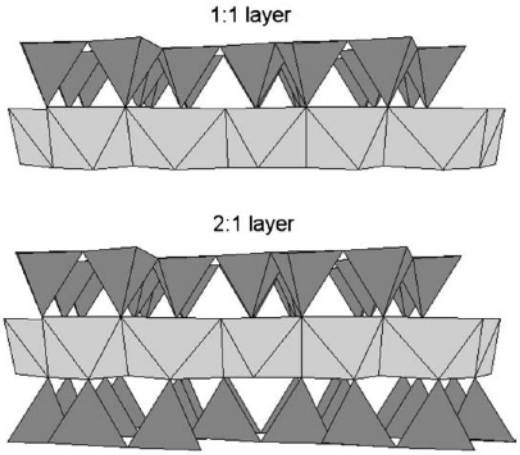


Figure 2.11: The 2:1 layer (top) and 1:1 layer (bottom). Figure adapted from [18].

molecules intercalated between the stacks that the regularity is lost. This process is normally not reversible.

### 2.8.1 Laponite

The clay mineral used in this thesis is Laponite RD. It is a synthetic smectite clay mineral with a 2:1 layered structure. The Laponite crystals are arranged into stacks that are held together electrostatically by shearing of sodium ions in the interlayer distance between adjacent crystals. The empirical formula for Laponite RD is shown in Figure 2.12.

The laponite particles are charged disk-like platelets. There is a negative charge on the faces of the particles because of the release of sodium ions, and the rims will be positively charged [19]. The platelets formed have a diameter of approximately 25 nm and a thickness of approximately 1nm.

Laponite is used as a rheology-modifier in many applications, for example in surface coatings, paints, household cleaners and personal care products.

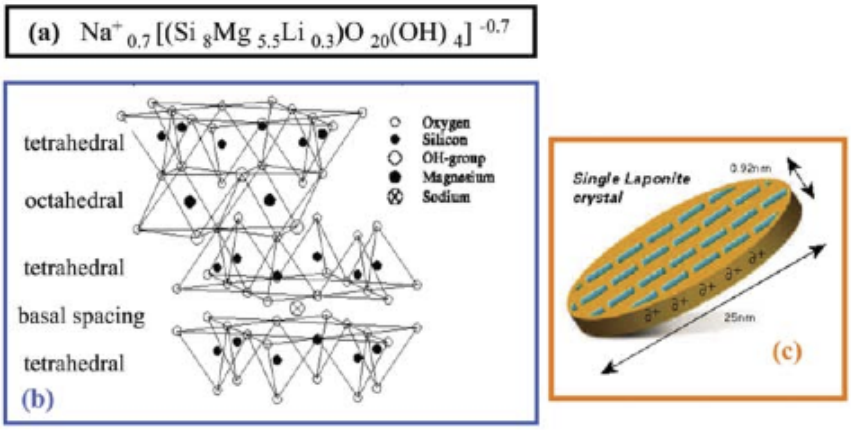


Figure 2.12: (a) Empirical formula for Laponite RD, (b) crystallographic structure of Laponite, and (c) single Laponite platelet. Figure adapted from [19].

### 2.8.2 Dipolar chain formations

Fossum et al.[20] investigated how clay particles dispersed in silicone oil behaved in an electric field. They found that when the suspensions are submitted to a strong external electrical field the particles form chains parallel to the applied field. This change appears fast, and the change coincides with a drastic change in rheological properties, which is why this type of suspensions sometimes are called electrorheological fluids. Figure 2.13 shows four different types of smectite clays between two copper electrodes with an applied field of $E \sim 500$ V/mm. The chains were formed after 10-20 s, and they found the critical field strength of $E_C \approx 400$ V/mm. For laponite suspensions this critical field strength has been found to be $E_C \approx 600$ V/mm [21].

The electric field induces electric dipoles in the clay particles, which with no applied field, has no dipole moment. By using synchrotron X-ray scattering it was found that the particles polarize along their silica sheet. Also a change in the platelet separation was found, which indicate that intercalated ions and water molecule play a role in the electric polarization of the particles.

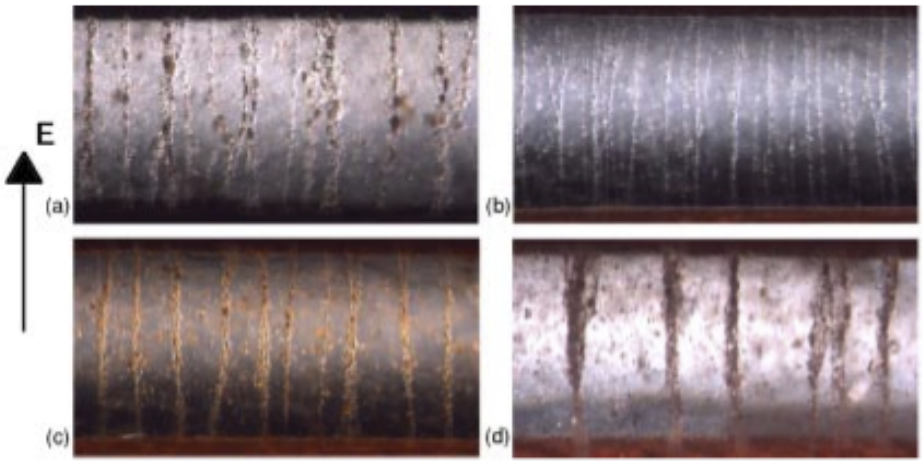


Figure 2.13: Microscope images of electrorheological chain formations in oil suspensions of smectite clays. (a) Na-fluorohectorite. (b) Ni-fluorohectorite. (c) Fe-fluorohectorite. (d) Natural quick clay. Figure adapted from [20].

## 2.9 Layered double hydroxides

Layered double hydroxides (LDHs), also known as anionic clays, are a class of layered materials discovered in Sweden in 1842 [22]. They have a structure that resembles clays, but they have an interlayer anion, not a cation like clays. They have many areas of application, including catalyst support and polymer stabilizers, and are facile and cheap to prepare [25].

The layer structures of most LDHs consist of metal hydroxide sheets and interlayers containing anions and water molecules. The metal hydroxide sheets can be dioctrahedral brucite ($Mg(OH)_2$) with a cation substitution such as $Al^{3+}$ instead of $Mg^{2+}$ to get positive charge, or it can be gibbsite sheets ($Al(OH)_3$) with $Li^+$ occupying vacancies [23]. They have interlayer anions to provide charge balance and also water molecules in the interlayer that form a hydrogen bond with the $OH^-$ groups as anions. The structure of a LDH that consist of brucite hydroxide sheets is shown in Figure 2.14

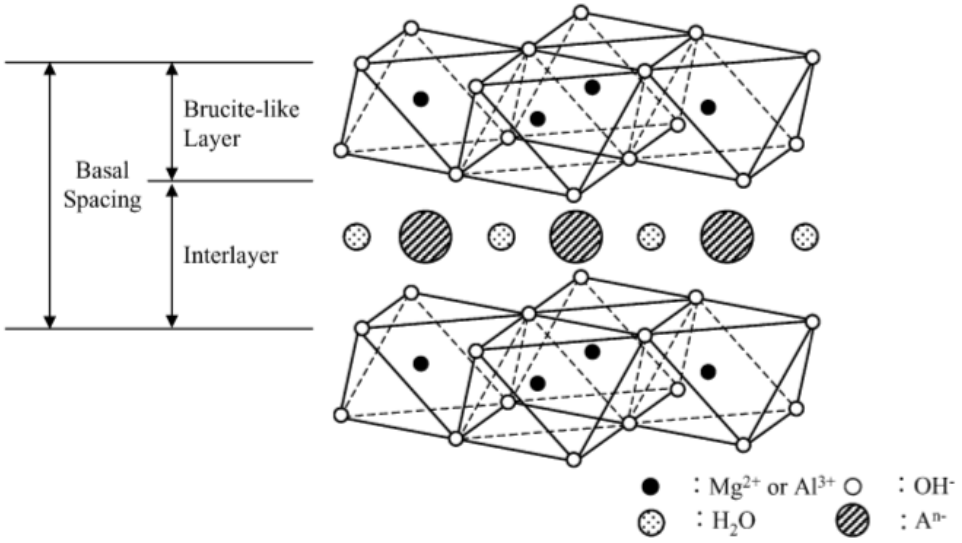


Figure 2.14: Schematic representation of Mg-Al LDH. Figure adapted from [24].

The LDHs possess a higher layer charge density than clays (2-5 meq/g), which causes strong electrostatic forces between the sheets and anions, thus

swelling is more difficult than for clays [26]. Hou et al. [23] did a study of the hydration properties of layered double hydroxides. Based on their results they divided the LDHs into three groups. (1) Significantly expendable (1.5-3.0 Å). This type of LDHs have very large inorganic anions intercalated, such as selenate ($SeO_4^{2-}$) or sulfate ($SO_4^{2-}$), and the fully expendable phases have a two water layer structure. (2) Slightly expendable ($< 0.5$ Å). Here, only one water layer is intercalated. (3) Essentially non-expendable (0-0.2 Å). These LDHs contains small and/or high charged anions, such as chloride ($Cl^-$) and carbonate ($CO_3^{2-}$), and will have very little interlayer water exchange.

# Chapter 3

# Experimental setup and procedure

## 3.1 Droplet production

To produce droplets a concentric flow cell was made in the lab. A sketch of the device is shown in Figure 3.1. A plastic tube with inner diameter 1.60 mm was used as the outer channel and a PEEK polymer tube from Upchurch Scientific with inner diameter 254 μm was used as the inner channel. Two Hamilton Gastight glass syringes of 25 ml and 10 ml were used to hold the dispersed and continuous phase. The plastic tubes were connected to the syringes by a three-way plastic tap, and silicone paste was used to avoid leakage.

The syringes were controlled by two COLEPALMER 78-0100C syringe pumps. An image of the concentric flow cell connected to the syringes and pumps is shown in Figure 3.2. The speed of the pumps was varied, and using flow rates of 40 ml/h for the continuous phase and 0.05 ml/h for the dispersed phase, droplets of $\simeq$ 350 μm were made. With these flow rates the droplet production was in the dripping regime and it was very stable, but because of the high viscosity and flow rate of the continuous phase, castor oil, there was produced a lot of satellite droplets. However, because we only needed to collect one or a few droplets this was not a problem, and the satellite droplets were collected and used, since droplets smaller than 350 μm was desired. An

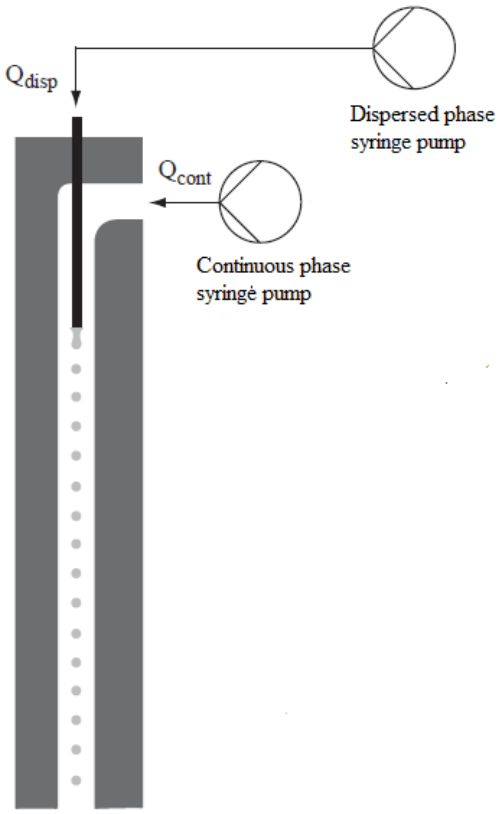


Figure 3.1: Sketch of the concentric flow cell used for making the droplets. Figure adapted from [15].

image of one droplet and one satellite droplet made with the same oil samples and the same flow rates is shown in Figure 3.3.

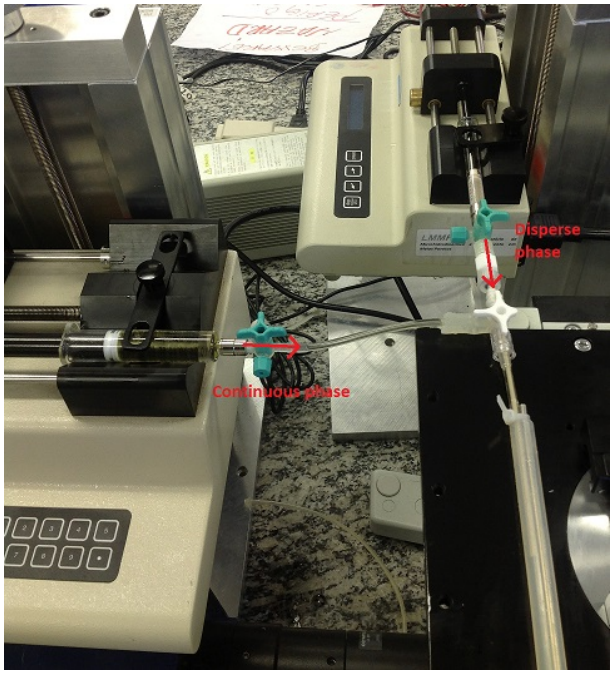


Figure 3.2: Image of the concentric flow cell connected to syringes and syringe pumps.

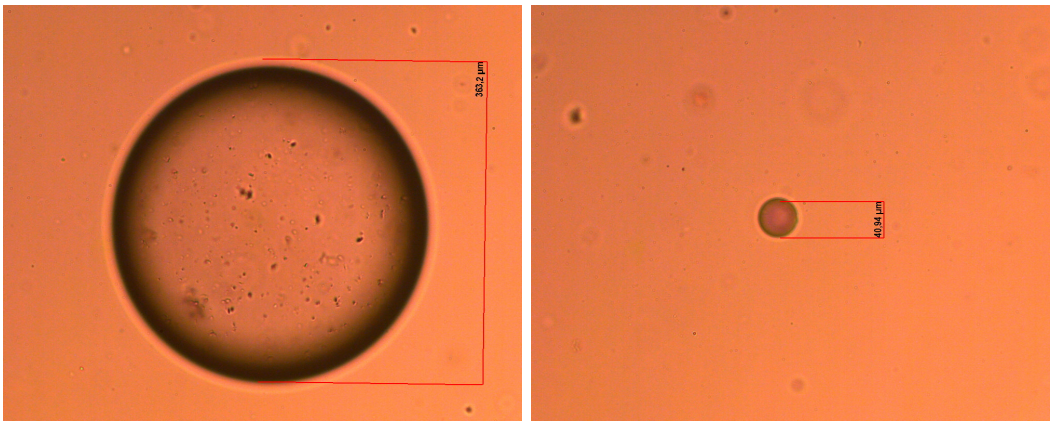


(a) (b)

Figure 3.3: Image of droplet and satellite droplet made with the concentric flow cell in the dripping regime. (a) Droplet with diameter 363 µm. (b) Satellite droplet with diameter 41 µm.

## 3.2 Experimental setup

Droplets were collected in a sample cell with two walls made of conductive ITO-glass (Indium Tin Oxide) and two sides with plexiglass walls. Three cells with different dimensions were used. One square cell with dimension 17.5 mm × 17.5 mm. The two others with dimensions 27.5 mm × 8 mm, where one of the cells had ITO-glass on the 8 mm walls, and the other with ITO-glass on the 17.5 mm walls.

A DC electric field was connected by crocodile clips to the ITO-glass. This was provided by a power supply connected to a power amplifier. Two different power supplies were used. One amplifier that gave a maximum output of 3 kV and one that gave a maximum output of 5 kV. Both amplifiers had output voltage dividers connected to a multimeter. The voltage divider to the amplifier that gave 5 kV did not work as expected, so the actual electric field strength in the experiments where this was used is not known exactly.

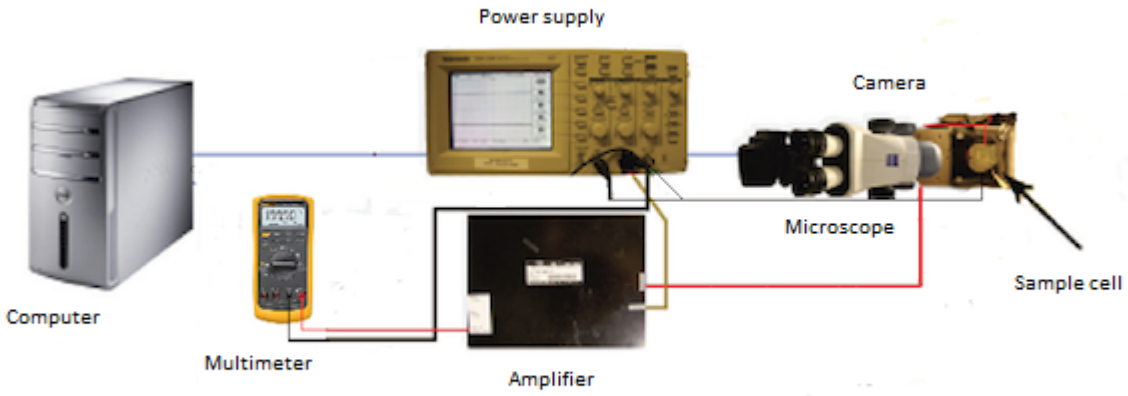


Figure 3.4: Illustration of the experimental setup.

A camera connected to a microscope was used to record the experiments. A CCD Monochrome Camera (Toshiba Teli CS8310BC) 752 × 582 pixels was used at first. Then it was exchanged by a Canon 600D camera that also

allowed for video capture. An illustration of the experimental setup is shown in Figure 3.4.

## 3.3 Sample preparation

The two oils used in this thesis were silicone oil for the droplets and castor oil as the surrounding fluid. The castor oil has specific density 0.961 g/cm$^3$ at 25°C, electric conductivity 45 pS/m, relative permittivity 4.7 and viscosity 1000 cSt. The silicone oil has specific density 0.97 g/cm$^3$, electric conductivity $\sim$ 3-5 pS/m, relative permittivity 2.1 and viscosity 100 cSt. For a silicone drop in castor oil, we then get R $\sim$ 0.1, S $\sim$ 2.2 and M = 10. These values should give oblate deformation according to Taylor's model for leaky dielectric drops, by the discriminating function given in equation 2.17. The interfacial tension between the two oils is 4.61 mN/m [16].

For the experiments with clay, Laponite RD was used. The clay and silicone oil was weighed and stirred with a magnetic stirrer for at least 24 hours. Since the clay doesn't swell in oil the stirring is very important to avoid large aggregations. In some of the experiments the sample was centrifuged and the top layer was used to avoid the largest aggregations. The silicone oil samples containing clay was put in one syringe and castor oil in the other, and the co-flowing device was used to make droplets.

Four different types of LDHs were used. (1) $Mg_3Al$-(TFA/Cl), containing 2 $TFA^-$ (trifluoroacetate) anions for each $Cl^-$ ion intercalated. (2) $Zn_3Al$-(TFA/Cl), containing 2 $TFA^-$ anions for each $Cl^-$ intercalated. (3) $Mg_3Al$-(Tf/Cl), containing 2 $Tf^-$ (trifluoromethanesulfonate) anions for each Cl- intercalated. (4) $Zn_2Al$-CMC, containing only CMC (carboxymethylcellulose) intercalated. The LDH was mixed with silicone oil either by hand shaking or with a magnetic stirrer. Drops of the silicone samples containing LDH were made with a high performance pipette, and placed in the middle of the sample cell already containing castor oil.

Samples with polyethylene and polystyrene beads were mixed in the silicone oil only by hand-shaking, to avoid crushing of the beads.

# Chapter 4

# Results and discussion

## 4.1 Clay ribbon

An equatorial clay ribbon formation was observed on droplets down to 45 μm radius, $\simeq$ 20 times smaller than the drops studied by Dommersnes et al. [3]. In Figure 4.1 the ribbon formation on a droplet with radius 65 μm is shown. Only 10 seconds after a DC field of 110 V/mm was applied the ribbon started to form. After about one minute the ribbon did not change any more, all the particles seemed to have migrated to the ribbon.

The thickness of the ribbon will depend on the initial clay concentration in the silicone oil sample used to make the droplet, but using the concentric flow cell to produce droplets made it difficult to predict the exact concentration of clay in the droplet. A lot of the clay sedimented in the syringe and the concentration in the droplets seemed to vary from drop to drop using the same sample. To avoid the problem with sedimentation some of the samples were centrifuged before put into the syringe. This way large aggregations of clay were avoided. However, centrifuging the samples also made it impossible to know the exact concentration of clay in the droplet, though a reproducible experiment was easier to obtain.

Assuming that the laponite aggregations have a width of a few micrometers, the concentration needed to cover the whole droplet surface can be calculated. Using that $d = cr/3$, where $d$ is the thickness of the film, $c$ is the clay

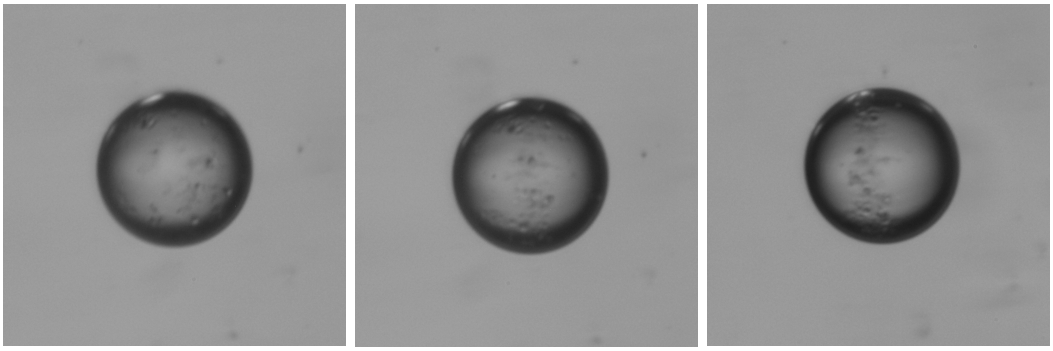

(a) Before. (b) 10 seconds. (c) 1 minute.

Figure 4.1: Clay ribbon formation on a droplet of radius $\simeq 65\,\mu$m with laponite particles. The field is perpendicular to the viewing direction. (a) Initially a lot of the clay is observed already on the surface before an electric field is applied. (b) A field of 110 V/mm is applied, and start of the formation of a ribbon can be seen after 10 seconds. (c) After ∼1 minute the ribbon is formed and does not change anymore.

volume concentration and $r$ is the radius of the drop, the volume concentration needed for a droplet with radius 50 μm is 18 %. Since the density ratio of clay and oil is $\sim$ 1.5-2 [3] the weight concentration needed to cover the droplet surface is $\sim$ 10 %.

There are two steps leading to the ribbon formation on the droplets. First, the clay particles have to migrate to the surface of the droplet and then, secondly, the ribbon is formed on the surface. On the droplets produced in the concentric flow cell, however, most of the clay particles were observed on the surface already before the electric field was applied. This happened because there will exist a lot of flow inside the channels while the droplets are being made, and some of this flow will lead particles to the droplet surface. Once the particles reach the surface they are likely to stay there, because of the surface tension between castor and silicone oil, $\gamma \simeq 4.5$ mN/m, which is high compared to thermal energies.

The particles left in the bulk of the droplet migrated to the surface after the electric field was applied. EHD flow cannot explain this migration, since it does not have a net component normal to the surface. The particles carried by the EHD flow will approach the surface, but turn before reaching it.

The time scale for a clay particle to diffuse 100 μm in 100 cSt silicone oil is $\sim$ 100 days, thus the only forces that may contribute to transporting the particles to the surface are electrical forces and/or gravitation. Since most of the particles were already on the surface of the droplet before the field was applied, these particles might have attracted the particles still in the bulk of the droplet, due to dipole-dipole interactions. There might also have been a charge uptake on the particles, causing them to move in the applied field, and hitting the surface. To study the influence on sedimentation some experiments using different sized insulating beads were done, discussed in section 4.3.

The formation of the ribbon once the particles were on the surface can however be explained by the EHD flow. Because of the conductivity and the dielectric properties of the oils used $RS < 1$, and the flow should resemble the one seen in Figure 2.2 (a). Following these flow lines the particles will form an equatorial ribbon on the droplet surface. Assuming that the particles follow the flow, i.e. that drag forces can be neglected, and that the clay concentration on the surface is not so big that it reduces the EHD flow, equation (2.18) can be used to find the time-scale for the particles to go to the ribbon, once they are on the surface. The time can be found by using $t \sim r/v_\theta$, where $r$ is the radius and $v_\theta$ the velocity of the EHD flow lines on the surface of the drop, given in equation 2.18. Dommersnes et al. [3] found it to be $t \sim 1.7 \times 10^5$ s $\times$ $(\mathrm{Vmm}^{-1}/E)^2$. The time scale will not depend on the size of the drop, since both the velocity and the time is proportional to the radius. This time scale for an applied field of 110 V/mm will be $\sim$ 14 s. This fits well for the droplet in Figure 4.1, since the clay particles on the droplet surface already started to form a ribbon after 10 seconds. This time scale, and the dependence of $E$ is further discussed in section 4.5.

No deformation is observed on the droplet in Figure 4.1. According to the discriminating function $\phi$, given in equation 2.17, there should be an oblate deformation for silicone oil drops dispersed in castor oil. Calculating the deformation, $D$, given in equation (2.16), for a pure silicone droplet of radius 65 μm in an applied field of strength 110 V/mm, gives $D \sim 10^{-4}$. This deformation, however, corresponds to a difference in $d_\perp$ and $d_\parallel$ less than 1 pixel in the images, so this will not be observable. The clay on the surface of the drop could have inhibited the EHD flow and thus the oblate deformation, since the clay is more conductive than both oils, hence reducing the charge build-up on the droplet surface. Because of this, experiments with pure

silicone droplets with a radius $\sim 50\,\mu m$ were done. No deformation was observed on these droplets either, which is as expected.

## 4.2 Clay pupil

A pupil-like was observed on droplets with a radius down to $80\,\mu m$. Figure 4.2 shows a droplet with a clay ribbon that closes when the field is increased. Increasing and decreasing the field can then be used to control the clay like an eye pupil that contracts and expands. The time it took for the pupil to contract and expand was not recorded, but it seemed to take a bit longer time than what was reported by Dommersnes et al. [3], who found a switching time of seconds.

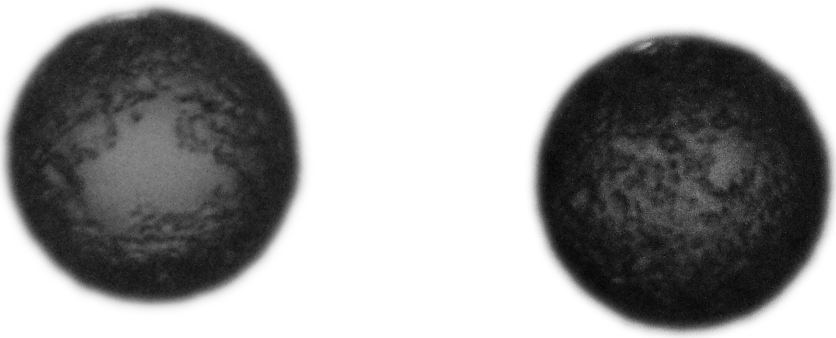

(a) (b)

Figure 4.2: Clay pupil on a silicone oil droplet with radius $\simeq 80\,\mu m$. The electric field is parallel to the viewing direction. (a) 2/3 of maximum field strength. (b) Maximum field strength.

This behaviour was only observed in experiments with clay, not with the insulating beads, and the effect can be explained by dipole-dipole interactions becoming more important at higher field strengths. When the electric field is increased, the clay form longer chains on the droplet surface. Since the

clay is more conductive than both oils, this will prevent charge build up on the drop surface and suppress the EHD flow. If the only mechanism was the EHD flow one would expect an increase in the flow when the applied field strength is increased, and thus narrowing the ribbon instead of widening it. For bigger drops, the fact that EHD flow is reduced can also be seen by looking at the deformation of the drop. The drop will change its form from oblate to prolate as the EHD is suppressed, but since the deformation of the droplets is so small this is not observed in these experiments.

## 4.3 Insulating colloidal beads

Ribbon formation was also observed on droplets where insulating polystyrene (PS) beads were used, as seen in Figure 4.3 . As with the droplets dispersed with clay particles made in the co-flowing channels, most of the particles were already on the surface before an electric field was applied. Most of the particles are on the top part of the droplet, because the silicone droplet has sedimented in the castor oil. Once the field was turned on, the ribbon started to form, and after 10 seconds the formation can be seen in Figure 4.3 (b). The ribbon here is very uneven, much broader on the top than on the bottom, because most of the particles were already at the top before the field was turned on. After some time, the ribbon became more even, seen in Figure 4.3 (c).

At the top of the droplet particles can also be seen to leave the surface. The PS particles seemed to be less attached to the surface than the clay particles, and since particles were very closely packed at the top of the droplet, some of the particles were released from the surface, and started to follow the EHD flows outside the droplet.

Even though the ribbon formed quickly, many particles moved for a while inside the droplet and it took about two minutes before all the particles reached the surface. It seemed to take longer time for all the particles to reach the surface for the PS particles than for the clay particles. This is the same that was reported by Dommersnes et al. [3] and supports the idea that the clay near the surface is attracted by dipole-dipole interactions to the particles that are already trapped at the interface. This effect will not be present with insulating beads, thus it takes longer time for all of the particles

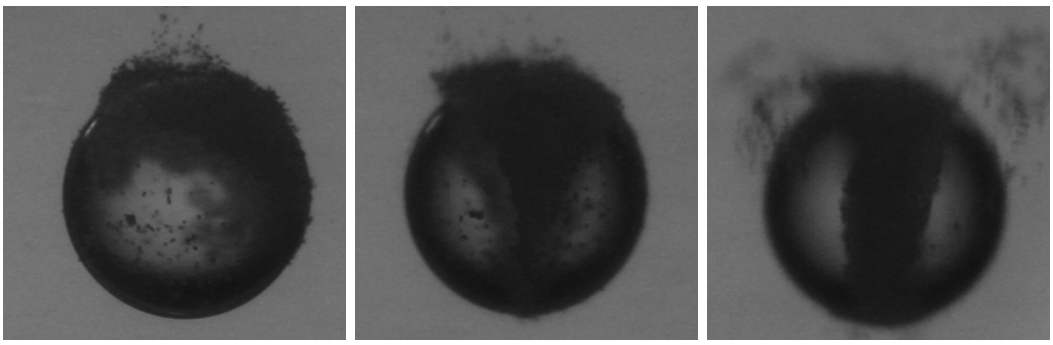

(a) (b) (c)

Figure 4.3: Ribbon formation on a silicone oil droplet of radius $\simeq 210\,\mu m$ with PS particles of 5 μm. The electric field is perpendicular to the viewing direction.

to reach the surface.

It seems to take a shorter time for the ribbon to form on the small droplets than for the millimeter sized ones, both for the clay ribbon and the ribbon made with insulating beads. Once the particles reach the surface, the time scale for forming the ribbon is expected to be the same as for bigger drops. The time for the particles to reach the surface might be expected to be shorter for the particles on the small droplets, if the particles are equal, since the sedimentation or electrical forces would be the same on the particles. However, for the experiments done here, the initial state was not the same as for bigger drops, and the fact that most of the particles were already on the surface will influence the time for the ribbon to form.

Also, rotating domains were observed in experiments using insulating beads. For high fields the ribbon breaks up into counter-rotating domains. At this point the mechanics of this instability is not fully understood, and needs further experimental study. An image of the rotating domain is shown in Figure 4.4.

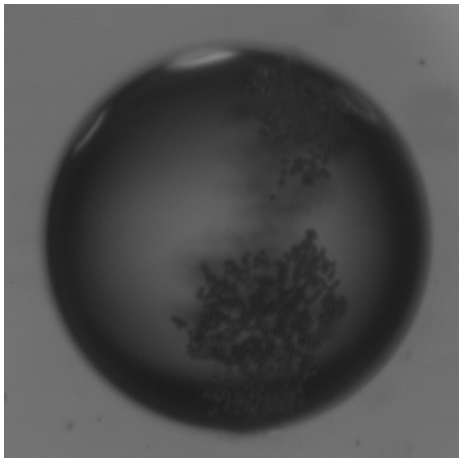

Figure 4.4: Silicone droplet with radius $\simeq 200\ \mu$m, with PS particles of size 5 $\mu$m. The image shows the ribbon that has been divided into several counter-rotating domains.

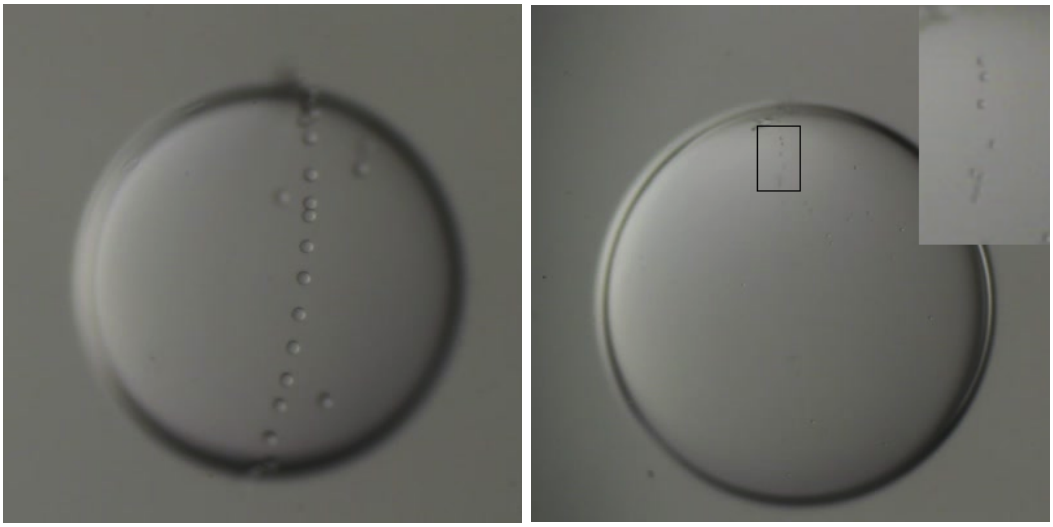

(a) (b)

Figure 4.5: Ribbon formation on drops with insulating PS beads 4 minutes after an electric field of 170 V/mm was applied. (a) PS beads of 50 μm diameter. Almost all particles are in the ribbon. (b) PS beads of 10 μm diameter. The ribbon is starting to be formed, but most of the particles have not reached the drop surface. The area in the square has been magnified to see the start of the ribbon formation better. The electric field is perpendicular to the viewing direction.

To study the influence sedimentation has in bringing particles from the bulk of the drop to the surface, experiments using different sized insulating polystyrene beads were done. Millimeter sized drops made with a pipette, dispersed with beads of 50 μm and 10 μm diameters were used. Figure 4.5 shows drops with the beads 4 minutes after an electric field with field strength 170 V/mm was applied. For the drop with the 50 μm beads the ribbon formation is easy to see, and only a few of the particles were still left in the bulk of the drop after 4 minutes. For the drop with 10 μm the start of the formation of the ribbon can be seen, but most of the particles did not reach the surface after 4 minutes. The drop itself sediments, and before the ribbon was formed on the drop with the 10 μm particles, the drop reached the bottom of the cell.

The ribbon made of the smaller particles takes a lot longer to form, and this

is an indication that sedimentation of the particles might be an important factor for the transport of the particles to the surface, but this needs to be studied further in order to say something certain. The fact that the drop itself sediment might influence the particles migrating to the surface. The idea was to do equivalent experiments using small droplets, but since making the droplets in co-flowing channels caused most of the particles to be on the surface already before the electric field was turned on, there was no point in doing this.

## 4.4 Coalescence of droplets

Coalescence of droplets has been observed, both with droplets dispersed with clay particles and with PS particles. Figure 4.6 shows the coalescence of two droplets with clay particles. First, the clay ribbon was formed on both the droplets. Then, from the position in Figure 4.6 (a), where the droplets were $\sim 3r$ apart, $r$ being the radius of the droplets, it took about a minute for them to be brought to a $2r$ distance. The droplets stayed this way for 40 seconds before they coalesced.

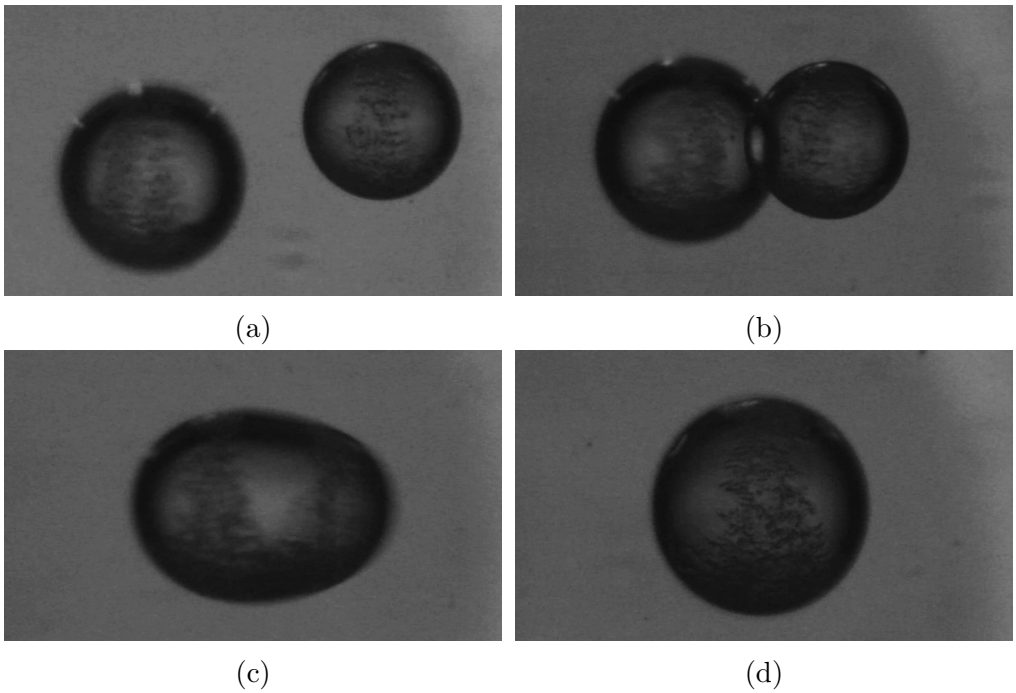

(a) (b)

(c) (d)

Figure 4.6: Coalescence of droplets with radius, $r \sim 100\,\mu$m. In (a) the distance between the droplets is $\sim 3r$. It takes about 1 minute for the droplets to move to a distance $2r$ in (b). They stay like this for 40 seconds before they coalesce in (c). In (d) the ribbon structure has once again been formed on the coalesced droplet. The electric field is perpendicular to the viewing direction.

For silicone oil drops in castor oil RS $< 1$, so the EHD flow around these droplets should create an attractive force. This attraction will dominate at

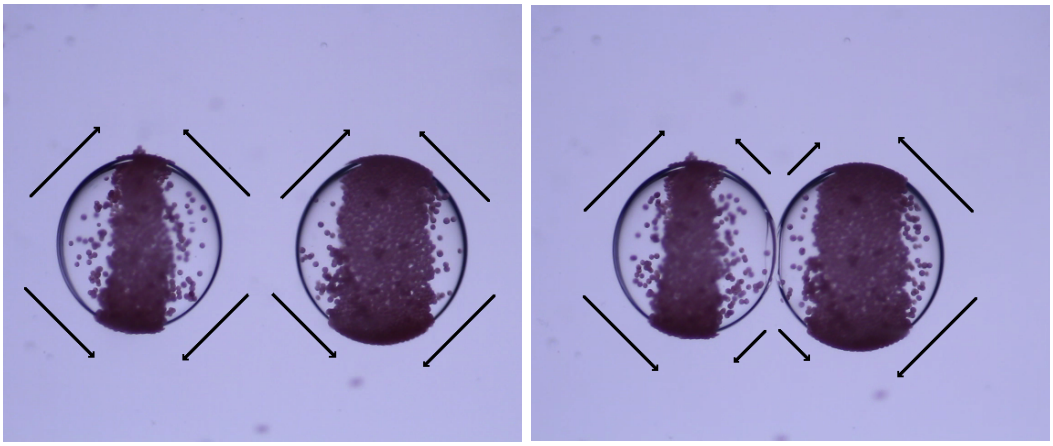

(a) $3r$ distance. (b) $2r$ distance.

Figure 4.7: Silicone oil drops dispersed with PE beads moves towards each other. (a) When the drops are $3r$ apart the flow is almost symmetric. As the drop moves closer it becomes more and more asymmetric, and in (b) when the drops are $3r$ apart, there is very little flow on the side of the drops closest to each other. Lines indicating the direction and size of the EHD flow outside the drops are drawn in the figure to illustrate what how the asymmetric flow causes the drops to move closer. The experiment was performed by Zbigniew Rozynek.

larger distances, and the closer the droplets are the more the electrophoretic attraction will dominate. The reason the EHD flow will make the droplets move towards each other is that when droplets are close enough to each other the flow lines between them are inhibited. In Figure 4.7 images from a video of two drops with PE beads are shown while they come closer, before they coalesce. Some of the PE beads were following the flow lines inside the drops. At first, when the drops were a distance $3r$ apart, flow that resembles EHD flow can be seen on both sides of the ribbon, in both drops. As the drops came closer, the flow became more asymmetric, the flow in between the drops became smaller. When the drops were $2r$ apart, there was very little flow in between the drops. Thus, the asymmetric flow pushes the drops together.

Once the droplets coalesce the ribbon was again formed on the surface of the coalesced droplet. For two equal sized drops the sum of the surface area of the two drops will be 25% bigger than the surface area of the coalesced

drop. This makes it possible, with a simple setup, to make jammed colloidal shells, by coalescing droplets that are not as packed with particles. By using different colloidal beads on the droplets, this controlled way of coalescing droplets can be used as a new method for making Janus shells. Some aspects of this are further discussed in the next section.

## 4.5 Assembly of colloidal particles on the drop surface

Experiments were done were done to detect the time it takes for the ribbon to be formed when the particles already are on the drop surface. Polyethylene (PE) beads with a diameter of 50 μm, dispersed in silicone drop with a radius of $\simeq 0.7$ mm were used. First, the beads were brought to the surface by applying a DC electric field. After this, the field was turned off, and by using a pipette the beads were spread on the surface. After each experiment the particles were spread on the surface again, so all the experiments were done with the same drop and same amount of PE beads.

In Figure 4.8-4.13 images of the drop with different electric field strengths applied are shown. The time to make the beads go to the ribbon was detected. By using that the average velocity $\langle v \rangle \sim r/t$, $r$ being the radius of the drop and $t$ the time, the average velocity was plotted as a function of the square of the electric field strength, shown in Figure 4.14.

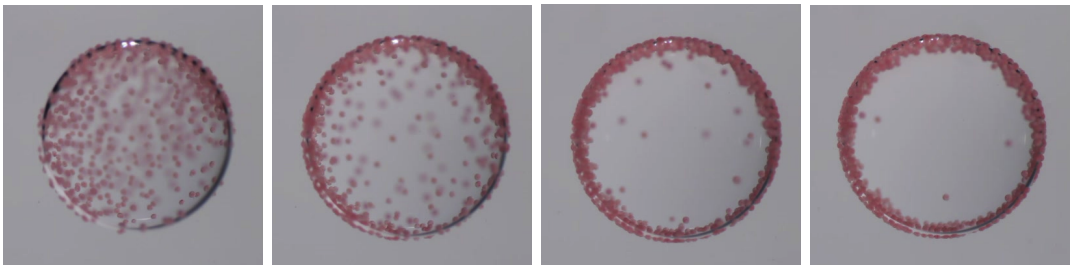

(a) Before (b) 1 second (c) 2 seconds (d) 3 seconds

Figure 4.8: Silicone oil droplet with r $\simeq 0.725$ mm with PE beads. The electric field is parallel to the viewing direction and has a strength of 400V/mm.

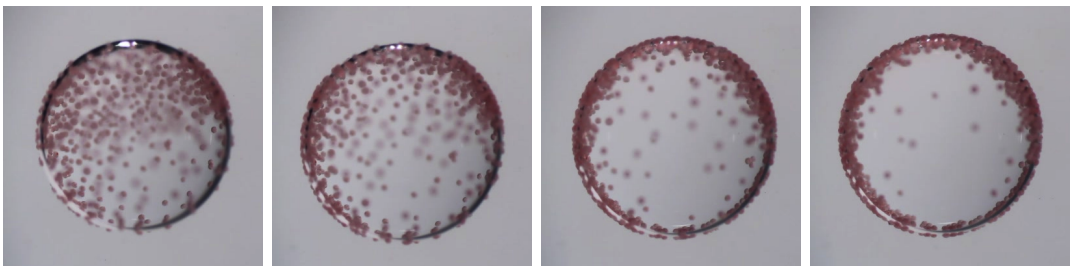

(a) Before (b) 1 second (c) 2 seconds (d) 3 seconds

Figure 4.9: Silicone oil droplet with r $\simeq$ 0.725 mm with PE beads. The electric field is parallel to the viewing direction and has a strength of 310V/mm.

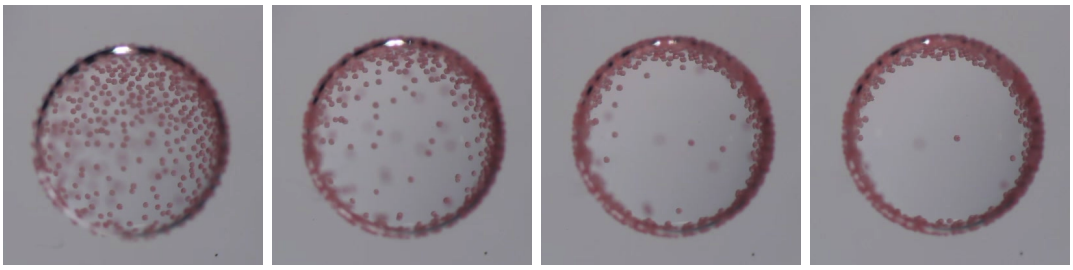

(a) Before (b) 2 second (c) 4 seconds (d) 6 seconds

Figure 4.10: Silicone oil droplet with r $\simeq$ 0.725 mm with PE beads. The electric field is parallel to the viewing direction and has a strength of 250V/mm.

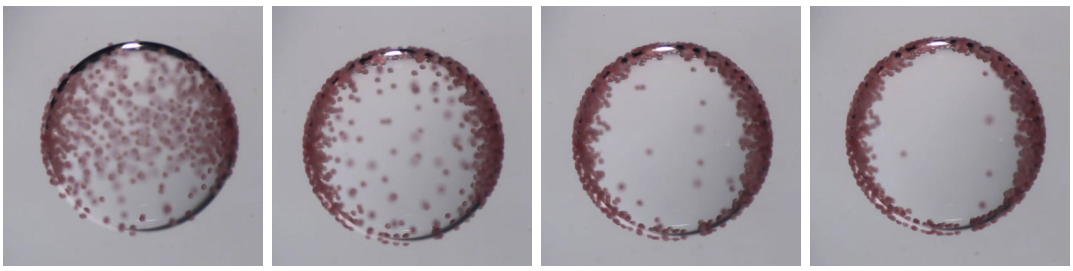

(a) Before (b) 4 seconds (c) 8 seconds (d) 12 seconds

Figure 4.11: Silicone oil droplet with r $\simeq$ 0.725 mm with PE beads. The electric field is parallel to the viewing direction and has a strength of 190V/mm.

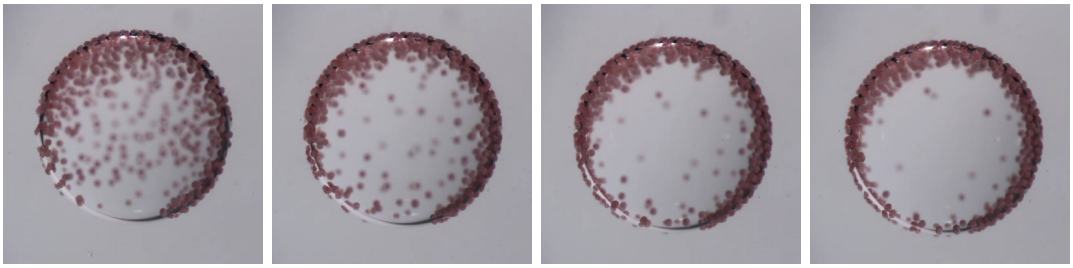

(a) Before (b) 5 seconds (c) 10 seconds (d) 15 seconds

Figure 4.12: Silicone oil droplet with r $\simeq$ 0.725 mm with PE beads. The electric field is parallel to the viewing direction and has a strength of 125 V/mm.

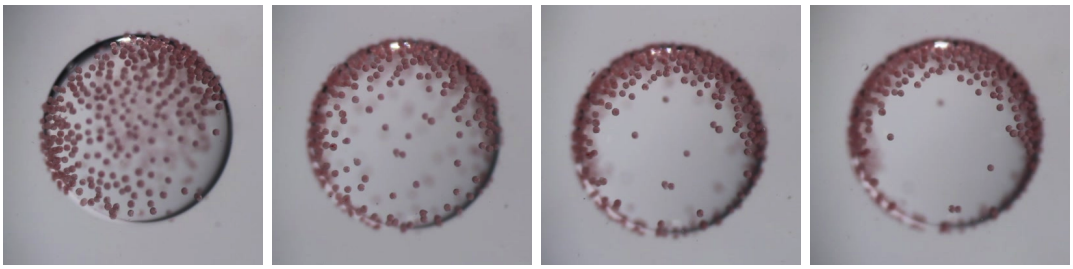

(a) Before (b) 1 minute (c) 2 minutes (d) 3 minutes

Figure 4.13: Silicone oil droplet with r $\simeq$ 0.725 mm with PE beads. The electric field is parallel to the viewing direction and has a strength of 60 V/mm.

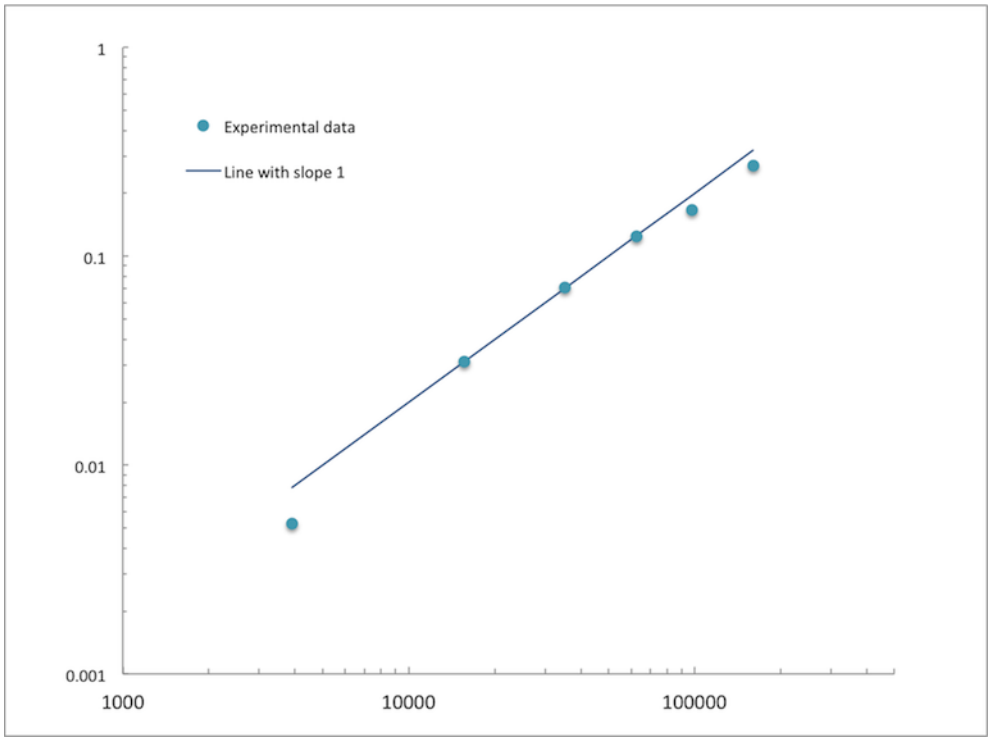


Figure 4.14: The average velocity of PE particles on the surface of a drop moving towards the equatorial ribbon, as a function of the square of the applied electric field strength $E^2$. The fitted curve has a slope of 1, which coincides with Taylor's prediction for the velocity of the EHD flow on the surface of a drop.

From Taylor's theory discussed in section 2.1, the velocity of the flow lines on the surface of a dielectric drop should go as $v_\theta \sim E^2$, as seen in equation (2.18). Assuming that the drag force can be neglected, the particles should follow these flow lines. Using that the time for the particles to go to the ribbon is $t \sim r/v_\theta$, the time is given by $t \sim 1.7 \times 10^5$ s $\times$ $(\mathrm{Vmm}^{-1}/E)^2$ [3]. For instant, for an applied field strength of 125 V/mm the time is $\sim$ 11 s. The time detected in experiments for this field strength was $\sim$ 22 seconds. The two numbers are of the same magnitude, and since the calculation is done using approximations the experimental value fits well.

Also, the velocity's dependence of $E^2$ fits well with the results. Figure 4.14 shows a linear relation between $v$ and $E^2$, which is what Taylor's model predicts. That the velocity depends on the electric field strength in this manner, makes it possible for a very fast assembly of the particles in the ribbon. This fast assembly of the particles can be important for a new way of producing Janus particles.

As already mentioned, a new way of preparing Janus colloidal shells could be by controlled electrocoalescence of drops. This method requires three steps. (1) The particles have to be brought to the surface of the drop. The method does not depend on how this is done. (2) The colloidal particles have to be assembled, to make them densely packed and to get them away from the electric poles, where they could prevent the coalescence. (3) The drops prepared in this way are then brought close enough together and exposed to a high enough electric DC field, which will make them coalesce. The experiments here show that step (2) can be done very fast and easily by applying a high electric field.

Thus, with a simple setup, jammed Janus colloidal shells can be made. Previously, the fabrication of Janus colloidal shells have only been done by using a flow-focusing microfluidic setup [35].

## 4.6 Experiments with layered double hydroxides

### 4.6.1 Visual experiments

In Figure 4.15 microscope images of the four different LDH samples dispersed in 10 cSt are shown. All the samples were shaken by hand and ultrasonicated. As seen in the images, the sample with $Zn_3Al$-(TFA/Cl) seems to disperse best in the oil. Also before ultrasonication, this sample was the only one that seemed to disperse in the oil, just by shaking the LDH powder in the silicone oil. It also looks like $Zn_2Al$-CMC is the sample that disperses the worst in silicone oil. Aggregations larger than 100 μm can be seen in this sample.

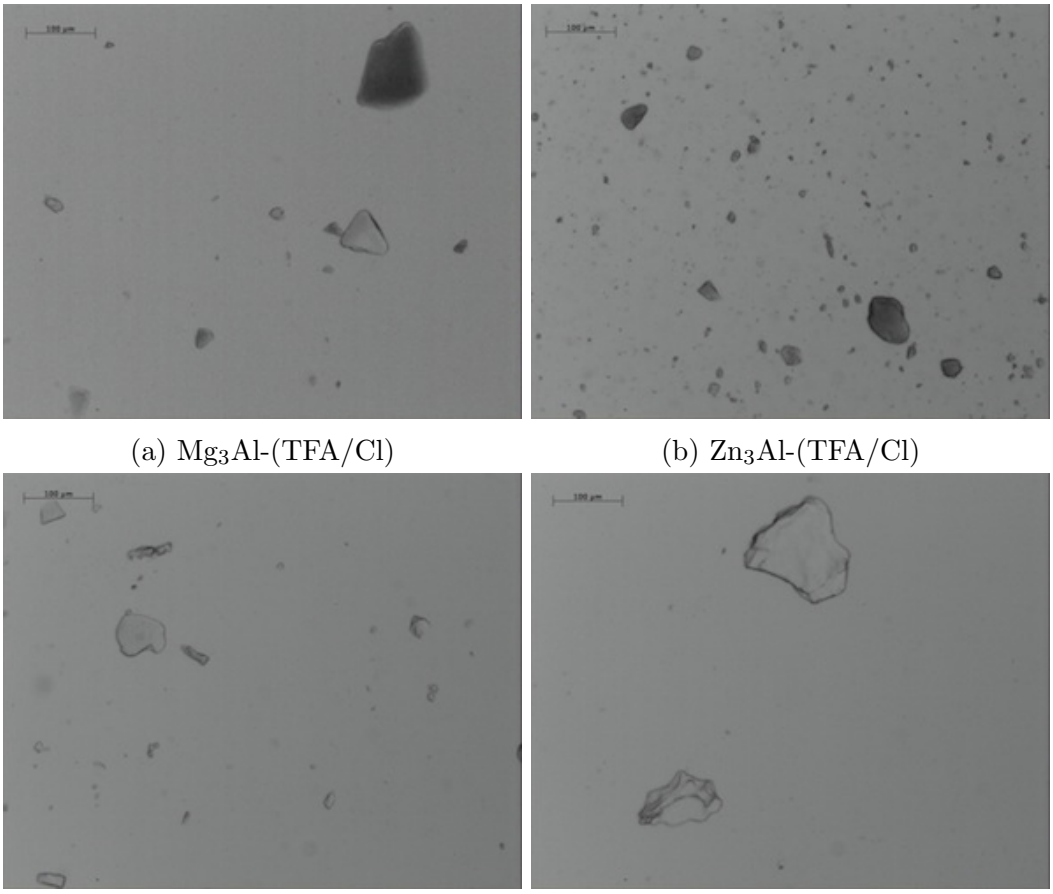

(a) $Mg_3Al$-(TFA/Cl) (b) $Zn_3Al$-(TFA/Cl)

(c) $Mg_3Al$-(Tf/Cl) (d) $Zn_2Al$-CMC

Figure 4.15: Microscope images of LDH samples dispersed in 10cSt silicone oil after ultrasonication. The scale bar is 100 μm in all images.

### 4.6.2 Chain formations

By placing one of the samples ($Zn_3Al$-(TFA/Cl) in 10 cSt silicone oil) on a glass plate between two electrodes and applying a DC electric field of 800 V/mm the particles formed chain-like structures shown in Figure 4.16. The chains were formed in the direction of the applied field, and looked a lot like the dipolar chains smectite clays form. The chains were formed quickly, but when the field was turned off nothing happened. Also, the chains were not even, and seemed to form branches close to the electrodes, which have not been observed in similar experiments with clays.

The behaviour that deviates from what has been observed in similar experiments with clay can be explained by way the experiments were performed. The sample was placed directly on a glass plate with electrodes glued to it on the sides. The surface might be uneven which could cause the particles to better stick to some areas, making the chains uneven. Also, there was observed some glue on the glass plate close to the electrodes, most of this on the places where most branching was observed. That the chains stayed the same way when the field was turned off is likely because the particles then were stuck to the glass plate, and would not move without some external force.

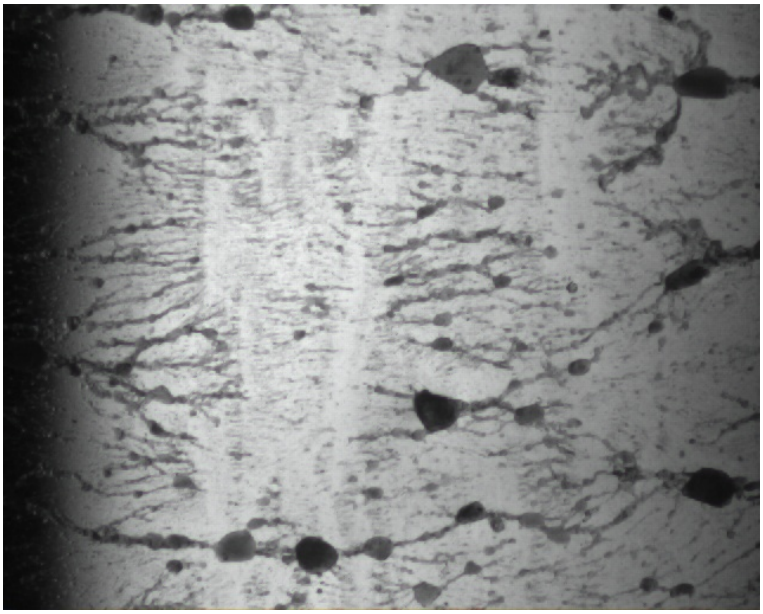

Figure 4.16: The dispersed sample of $Zn_3Al$-TFA in 10 cSt silicone oil put on a glass plate between a DC electric field of field strength 800 V/mm. The particles form chains quickly.

### 4.6.3 Droplets in DC field

Using LDHs dispersed in 100 cSt silicone drops in castor oil, and applying a DC electric field, resulted in many of the same phenomena observed with clays. Ribbons, chains, pupils and rotating domains were observed. The amplifier used in these experiments (except the experiment that showed a pupil-like effect), should give a maximum field strength of 5000V ($\simeq$ 290 V/mm), but the voltage divider was broken, so the exact field strength is not known.

For three of the samples, $Mg_3Al$-(Tf/Cl), $Mg_3Al$-(TFA/Cl), $Zn_3Al$-(TFA/Cl), ribbon formation was observed. For the fourth sample, $Zn_2Al$-CMC, only chain formations were observed on the drop surface when a DC electric field was applied. For $Mg_3Al$-(Tf/Cl), one sample that was hand-shaken only showed chain formation once the field was applied (Figure 4.19), while the same sample, left stirring with a magnetic stirrer for 2 hours showed ribbon formation with the same applied field (Figure 4.18).

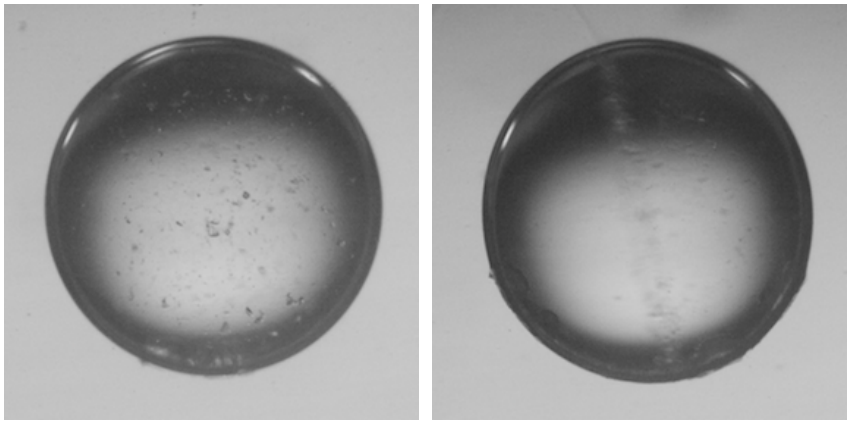

(a) Before applying field. (b) Maximum field strength.

Figure 4.17: Silicone oil droplet of size $\simeq$ 0.7 mm with $Mg_3Al$-(Tf/Cl) concentration of 1 wt%. In (b) the particles have formed a thin ribbon on the surface of the drop after an electric field is applied. The electric field is perpendicular to the viewing direction.

The ribbon formation on the drop in Figure 4.18 moved when the electric field strength was increased. At half of maximum field strength it can be seen to be a bit shifted away from the positive electrode, and when the field

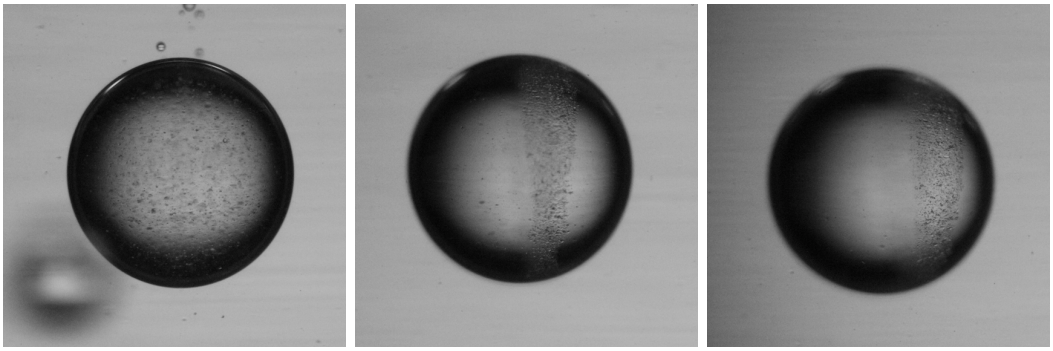

(a) Before applying field. (b) Half of max field. (c) Maximum field.

Figure 4.18: Silicone oil droplet with radius of $\simeq$ 0.7 mm with $Mg_3Al$-(TFA/Cl) concentration of 1 wt%. This sample was stirred with a magnetic stirrer for 2 hours. In (b) a ribbon has been formed after applying an electric field, and in (c) the ribbon has shifted when a higher field is applied. The electric field is perpendicular to the viewing direction.

strength was increased to maximum the ribbon shifted even more. There is no obvious explanation for the behaviour at this point, but similar behaviour has been observed in experiments with modified clay [1].

There is clearly a correlation between the size of the particles and the formation of a ribbon or chains on the surface. By looking at the microscope images in Figure 4.15 we see that $Zn_2Al$-CMC and $Mg_3Al$-(TFA/Cl) are the samples with largest particle sizes, and also the samples where only chain formation was observed before stirring. Also, by looking at the drops in Figure 4.17 - 4.20 it is clear that the drops with the smallest particles form ribbons and the biggest form chains. For the drops in Figures 4.18 and 4.19 equal samples were prepared, but the sample in Figure 4.18 was stirred, and had smaller particle aggregations than the sample used for the drop in Figure 4.19 that was not stirred. The same field was applied, so the only difference was the size of the aggregations. The particles on the drop with the smallest aggregations formed a ribbon, while the particles on the drop with the biggest aggregations formed chains that stretched across the whole drop surface.

The dipole moment induced on a particle is proportional to the size of the particle, which explains the behaviour observed. Because of the high dipole moment induced on the large particles, the particles form chains easier, and

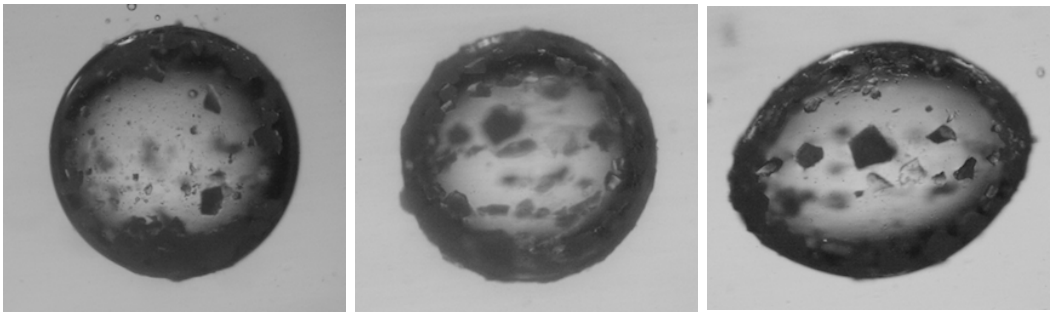

(a) Before applying field. (b) Half of max. field. (c) Maximum field.

Figure 4.19: Silicone oil droplet with radius $\simeq 0.7$ mm with $Mg_3Al$-(TFA/Cl) concentration of 1 wt%. In (b) and (c) chains of particles are observed on the surface, and in (c) where the field strength is twice the value as in (b) the drop takes an oblate form. The electric field is perpendicular to the viewing direction.

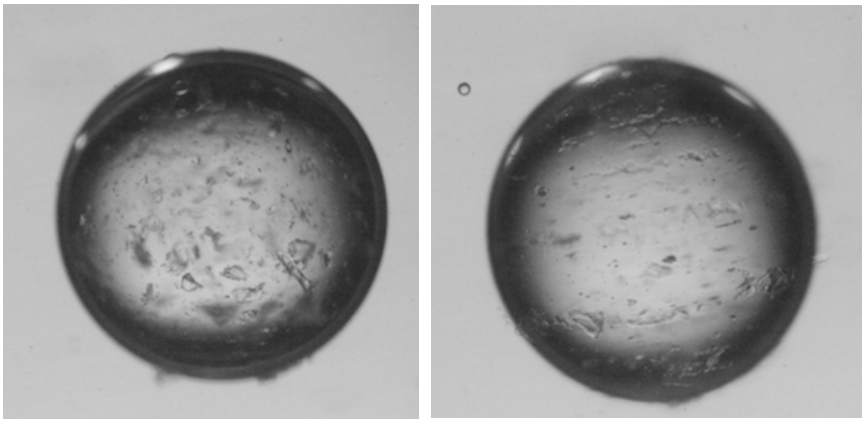

(a) Before applying field. (b) Maximum field.

Figure 4.20: Silicone oil droplet with radius $\simeq 0.6$ mm with 1 wt% of $Zn_2Al$-CMC. After applying a DC electric field the particles form chains on the drop surface. The electric field is perpendicular to the viewing direction.

when the field is high the like in Figure 4.19 (b) the drop is stretched toward the electrodes, and have a prolate form. Thus the size of the particles influences the deformation of the drops. For a drop dispersed with small particles, the EHD flow is dominant, and will cause oblate deformation of the drop. For a drop dispersed with larger particles, the effect of the dipole moment will be dominant, the EDH flow is suppressed, and the drop obtain a prolate deformation.

However, it is not just the size of the particles that decide how a drop is deformed. As seen in Figure 4.19 an increase in the electric field clearly increases the prolate deformation when the drop is covered with chains on the surface. Also the concentration of particles is important. In Figure 4.21 the initial concentration of particles on the drop was very high, and when an electric field was applied the drop deformed prolately. Left like this for a while the particles were attracted to the electrodes and can be seen to leave the surface of the drop. Hence, after a while the concentration on the drop surface is less than the initial concentration, and the drop is no longer prolately deformed. The reason the high concentration of particles makes the drop prolate is because the EHD flow is reduced because the particles on the surface of the drop is more conductive than both the silicone and castor oil, and thus prevents charge build-up on the drop surface.

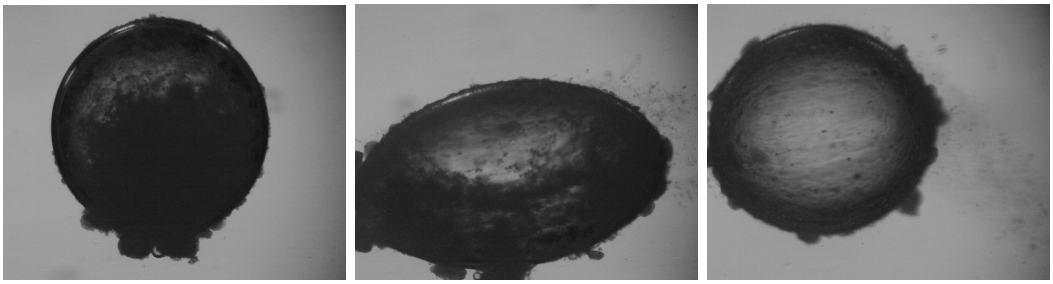

(a) Before applying field. (b) Maximum field. (c) Maximum field.

Figure 4.21: Silicone oil droplet with radius $\simeq$ 1 mm with $Zn_3Al$-(TFA/Cl) concentration of 1 wt%. (a) The concentration of particles on this drop is very big before the DC field is turned on. (b) The drop has got a prolate shape after the field is turned on. After a while a lot of the particles has been attracted to the electrodes and disappeared from the drop, and in (c) the drop can be seen with less particles, and the drop is not as prolately deformed any more.

Also a pupil-like effect was observed, where an increase in the electric field strength caused the ribbon to stretch. This seems to be in accordance to what has earlier been observed with clays. This effect is shown in Figure 4.22.

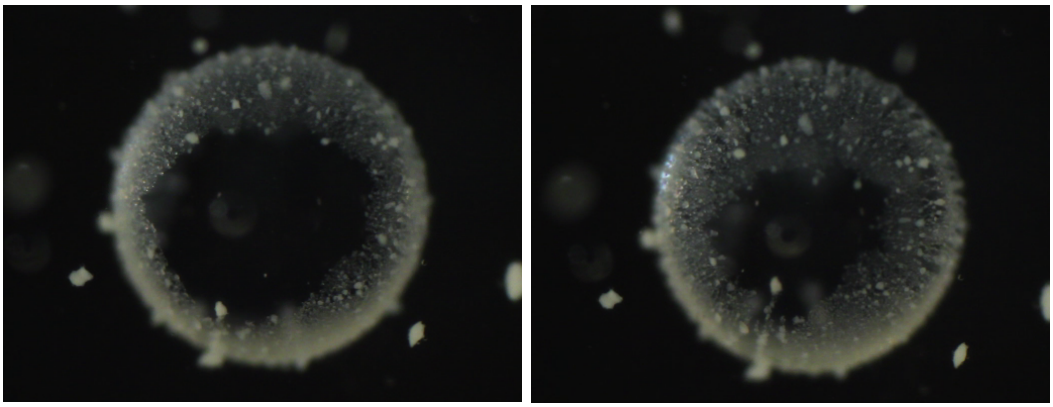

(a) (b)

Figure 4.22: Silicone oil droplet with radius $\simeq 0.7$ mm with $Zn_3Al$-(TFA/Cl) concentration of 2 wt%. An electric field with strength 180 V/mm is applied parallel to the viewing direction and a LDH ribbon is formed on the drop in (a). By increasing the electric field strength to 360 V/mm in (b) the ribbon is stretched and the particles cover more of the surface.

## 4.7 Uncertainties

There will be an uncertainty regarding the concentration of particles in droplets made using the concentric flow device. The clay particles sedimented in the syringe, making the concentration in the droplets less than the concentration in the silicone oil sample. Some of the samples were centrifuged before putting them in the syringe avoiding the largest clay aggregates, though this way the actual concentration of clay in the droplets would not be known either.

Another is the electric field strength in some of the experiments. To get higher field strength the voltage amplifier that gave maximum field strength

of 3 kV was exchanged for one that gave maximum 5 kV. To be able to monitor the voltage coming out of the amplifier, it was connected to a voltage divider and then a multimeter, since the multimeter could only take an input up to 1 kV. However, for lower voltage, where it could be measured directly by the multimeter, the voltage divider did not give out the output it was supposed to. Therefore, it is uncertain what the real voltage was in the experiments were this voltage amplifier was used. Because of the behaviour of the drops and particles, compared to using the amplifier that gave maximum of 3 kV, it is believed that the field was higher than than 3 kV. In the experiments where this amplifier is used the field strength is given as "maximum field strength", "half of maximum field strength", etc.

# Chapter 5

# Conclusion and future studies

## 5.1 Concluding remarks

Experiments showed that colloidal particles dispersed in small leaky dielectric droplets give similar structure to particles on drops $\sim 20$ times larger, when a DC electric field is applied. Ribbon formation and pupil-like effects were observed in experiments involving clay particles, and ribbon formation and rotating domains were observed in experiments involving insulating beads. It is difficult to compare the time it takes to form the ribbon on the small droplets with the time it takes on the bigger drops. This is due to droplet formation in microfluidic channels causing most of the particles to go to the surface before any electric field is applied. However, the time-scale for assembly of the particles on the drop surfaces is not expected to depend on the drop size, and this time seems to fit well with theory. Also, for the small droplets, there seemed to be some difference in the way the ribbon was formed between experiments using clay particles and those using insulating beads. The insulating beads were observed circulating longer inside the droplets than the clay particles, which is the same that has been reported earlier for bigger drops. This supports the theory that electrical forces contribute to transporting the particles to the drop surface.

Other experiments done with bigger drops, made with a pipette, indicated that sedimentation is important for bringing the particles to the surface. Experiments with different sized insulating beads showed that it takes longer

time to create the ribbon on the drop with the small beads than on the big ones. However, other effects, like sedimentation of the drops, are not taken into account. This needs to be studied further in order to say something certain.

Coalescence of droplets, due to electrophoretic and EHD effects, has been observed. As the distance between the drops decreases, the EHD flow becomes antisymmetric, which then pushes the droplets together.

Experiments using insulating beads on a drop surface showed that the relation $v \sim E^2$, given in the leaky dielectric model, for the velocity of the EHD flow on the surface of the drop, fits very well with the experiments. This enables fast assembly of particles on the drop surface, which is important in a new method for making jammed Janus shells, through coalescence of drops.

LDH particles, that have a structure similar to clays, were found to behave similar to clay particles in the experiments performed. With LDH particles dispersed in silicone oil, chain formation was observed when a DC electric field was applied. Ribbons, chains, pupils and rotating domains were observed in experiments using LDH particles dispersed in leaky dielectric drops. The size of the particles seems to influence whether a ribbon or chains are formed on the surface, and this way the size also influences the deformation of the drops. This is all in accordance with what has been observed in experiments previously involving clay particles.

## 5.2 Future studies

The influence sedimentation has on transporting particles to the surface of the drop is still not fully understood, and should be studied further. Some experiments were done to investigate this, where the time it took to form the ribbon with different sized PS beads was recorded. The smallest particles did not form the ribbon before the drop had sedimented to the bottom of the sample cell, which made it difficult to do quantitative studies. However, it did give an indication that the ribbon of smaller particles takes longer time to form. For future studies it would be a good idea to use smaller droplets, if these can be produced without causing many of the particles to go to the

droplet surface before the field is applied. Using smaller droplets would make the droplet sediment much slower, which gives more time to observe what happens. Additionally this would make the effect the sedimentation of the drop has on the particle migration negligible.

In the experiments done with LDH particles there was clearly a correlation between the size of the particles and the deformation of the drops, and it would be interesting to the study this further and find the exact relation. The reason for this correlation is that bigger particles easier form dipolar chains, and the EHD flow is reduced. To be able to do this exactly, the particles used would have to be polarizable and form dipolar chain structures on the drop surface, and control of the particle size would be necessary.

# Appendix A

# Detailed calculation of dielectric sphere in electric field

This calculation shows the details that leads to equation (2.4) and (2.5) in the theory section. The calculation follows the calculation in *Introduction to electrodynamics* by Griffiths [4].

In spherical coordinates, Laplace's equation is given by

$$\frac{1}{r^2}\frac{\partial}{\partial r}\left(r^2\frac{\partial V}{\partial r}\right)+\frac{1}{r\sin\theta}\frac{\partial}{\partial\theta}\left(\sin\theta\frac{\partial V}{\partial\theta}\right)+\frac{1}{r^2\sin^2\theta}\frac{\partial^2 V}{\partial\phi^2}=0 \tag{A.1}$$

In our problem, the potential $V$ will be independent of $\phi$. It has *azimuthal symmetry*, and equation (A.1) is written as

$$\frac{1}{r^2}\frac{\partial}{\partial r}\left(r^2\frac{\partial V}{\partial r}\right)+\frac{1}{r\sin\theta}\frac{\partial}{\partial\theta}\left(\sin\theta\frac{\partial V}{\partial\theta}\right)=0 \tag{A.2}$$

Using the method of separation of variables we look for solutions on the form

$$V(r,\theta)=R(r)\Theta(\theta) \tag{A.3}$$

Using this in equation (A.2) and dividing by V

$$\frac{1}{R}\frac{d}{dr}\left(r^2\frac{dR}{dr}\right)+\frac{1}{\Theta\sin\theta}\frac{d}{d\theta}\left(\sin\theta\frac{d\Theta}{d\theta}\right)=0 \tag{A.4}$$

Since the first term only depends on $r$ and the second only on $\theta$, they must both be constant and can be written like

$$\frac{1}{R}\frac{d}{dr}\left(r^2\frac{dR}{dr}\right)=l(l+1) \tag{A.5}$$

and

$$\frac{1}{\Theta\sin\theta}\frac{d}{d\theta}\left(\sin\theta\frac{d\Theta}{d\theta}\right)=-l(l+1) \tag{A.6}$$

The radial equation, equation (A.5), has the solution

$$R(r)=Ar^l+\frac{B}{r^{l+1}}, \tag{A.7}$$

where A and B are arbitrary constants. There are two solutions to the angular equation, equation (A.6), where one of them are the *Legendre polynoms* in the variables $\cos\theta$

$$\Theta(\theta)=P_l(\cos\theta) \tag{A.8}$$

The second solution is not valid physically, because it blows up at $\theta=0$ and/or $\theta=\pi$. Therefore, the most general separable solution to Laplace's equation is

$$V(r,\theta)=\left(Ar^l+\frac{B}{r^{l+1}}\right)P_l(\cos\theta) \tag{A.9}$$

Since separation of variables gives an infinite number of solutions, one for each value of $l$, the *general* solution is a superposition of these solutions

$$V(r,\theta) = \sum_{l=0}^{\infty} \left( Ar^l + \frac{B}{r^{l+1}} \right) P_l(\cos\theta) \tag{A.10}$$

To find the solutions in our problem we use the boundary conditions

$$\begin{aligned} &V_{in} = V_{out},\ r = R, \\ &\epsilon \frac{\partial V_{in}}{\partial r} = \epsilon_0 \frac{\partial V_{out}}{\partial r} \\ &V_{out} \to -E_0 r\cos\theta,\ r >> R, \end{aligned} \tag{A.11}$$

From equation (A.10) we see that the potential inside the sphere has to be

$$V_{in}(r,\theta) = \sum_{l=0}^{\infty} A_l r^l P_l(\cos\theta) \tag{A.12}$$

and using boundary condition (iii) the potential outside the sphere has to be

$$V_{out}(r,\theta) = -E_0 r\cos\theta + \sum_{l=0}^{\infty} \frac{B_l}{r^{l+1}} P_l(\cos\theta) \tag{A.13}$$

Using (i) we get

$$\begin{aligned} A_l R^l &= \frac{B_l}{R^{l+1}},\ \text{for l } \neq 1 \\ A_1 R &= E_0 R + \frac{B_1}{R^2} \end{aligned} \tag{A.14}$$

and from (ii)

$$\begin{aligned} \epsilon_r l A_l R^{l-1} &= \frac{(l+1)B_l}{R^{l+2}},\ \text{for } l \neq 1 \\ \epsilon_r A_1 &= -E_0 - \frac{2B_1}{R^3} \end{aligned} \tag{A.15}$$

Thus, we find that

$$\begin{aligned} A_l &= B_l = 0, \text{ for } l \neq 1 \\ A_1 &= \frac{3}{\epsilon_r + 2} E_0, \; B_1 = \frac{\epsilon_r - 1}{\epsilon_r + 2} \end{aligned} \tag{A.16}$$

Hence, the potential inside the sphere is given by

$$V_{in}(r, \theta) = -\frac{3E_0}{\epsilon_r + 2}, \tag{A.17}$$

and the potential outside the sphere is

$$V_{out}(r, \theta) = \left( \left( \frac{\epsilon_r - 1}{\epsilon_r + 2} \right) \frac{R^3}{r^2} - r \right) E_0 \cos\theta, \tag{A.18}$$

# Appendix B

# Report: Parameters affecting the droplet formation in microfluidic concentric flow cells

# Parameters affecting the droplet formation in microfluidic concentric flow cells

Julie Janine R. Seth and Emilie L. Johnsrud

June 24, 2013

## 1 Introduction

Microfluidic devices have become increasingly important in the field of monodisperse droplet production. One way of doing this is using a concentric flow channel, in which the dispersed phase is injected via a needle or a tube into another co-flowing, immiscible fluid which makes up the continuous phase. Figure 1 illustrates a typical geometry for such a device. The formation of drops in concentric flow channels can be done in two ways. Drops formed close to the capillary tip is called dripping, while the breaking up of an extended jet is called jetting. In general, the dripping mechanism is a result of force balance between interfacial tension and drag forces, while drop formation in the jetting regime is a result of Rayleigh instabilities. Rayleigh instabilites are a result of perturbations leading to break up of the jet because of surface tension forces. The dynamics change significantly at the transition point between these two mechanics, which is often defined as the point where the initial rise velocity of a drop is sufficiently low that the drop will grow less than one drop diameter during the time of formation of the next drop. It has been found that critical jetting velocity is dependent on whether one starts from the jetting regime and decreases the flow of the dispersed liquid, or one starts in the dripping regime and increases the disperse flow rate [3].

In the dripping mode the primary drops have been found to have very high monodispersity, and is therefore of high engineering interest. Umbanhowar et al.[2] found polydispersities smaller than 3%. The formation of droplets in the dripping mode can be divided into two stages, (1) stable growth at the

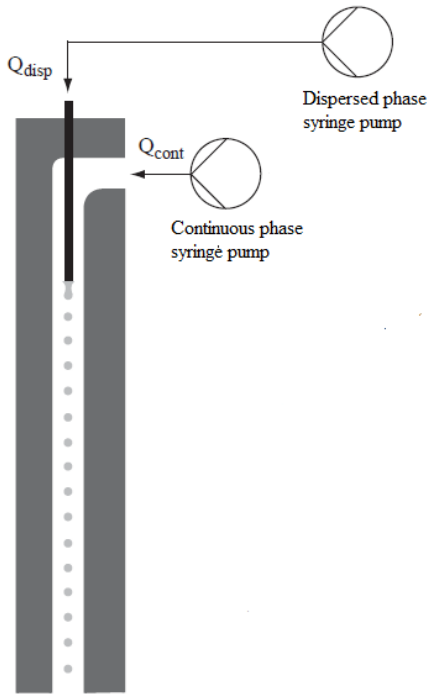


**Figure 1:** An illustration of a concentric flow cell. Adapted from [1].

capillary that ends with loss of equilibrium of the forces and is followed by (2) necking and detaching of the drop. At high viscosities a thread between the primary drop and the capillary is formed and this leads to the formation of satellite drops. After the breakup of the primary drop, small satellite drops are formed because of secondary breakup of the thread due to unbalanced capillary forces.

The parameters influencing the droplet sizes are flow rates, viscosities and densities of the continuous and dispersed phases, interfacial tension and the sizes of the channel and the capillary. At the micrometer scale used in these kinds of geometries, the relative effect of viscous forces to interfacial tension forces are the most important as they dominate inertial and gravitational forces.

# 2 Effect of flow rates

Cramer et al. [1] studied the effect of flow rates focusing on the dripping mode and the transition between dripping and jetting. All the experiments were done with refined sunflower oil as the continuous phase, with a viscosity of 0.049Pa s and a density of 916kg/$m^3$. The dispersed phase varied since they also wanted to study how the drop size depended on the viscosity and interfacial tension. Most of the experiments were done in a with an outer flow channel of hight 20mm and width 2.5 mm. The inner diameter of the steel channel where the dispersed phase was injected was 0.1mm and the outer diameter was 0.3mm. With this channel drops larger than 0.2mm was generated. They also made a smaller channel for generation of droplets smaller than 0.1mm. This flow channel had a height of 2mm and a width of 1 mm, and a glass capillary of inner diameter 0.02 mm was used for the injection of the dispersed phase.

## 2.1 Transition from dripping to jetting

The transition between dripping and jetting in a co-flowing liquid-liquid system will depend on the rate of both the continuous and dispersed phase, and it will correlate with the continuous flow rate when all other parameters are held constant. Figure 2 shows drop diameter around the transition as a function of the continuous phase velocity found by Cramer et al. It was observed that small disturbances could provoke the generation of a jet, so to make the results reproducible all the experiments were done starting with high velocities in the jetting mode. This behavior has been observed previously by Clanet et al. [3] who found different jetting velocity for liquid injected into air depending on whether one starts from the jetting or dripping regime.

Figure 2 shows that the diameter of the droplet decreases with increasing flow rate of the dispersed rate because of an increased drag force in the continuous fluid. When $v_{cont}$ is increased the detatchment time will be smaller, and thus there will be a decrease in the diameter of the drops. The velocity at the transition between the dripping and jetting mode was found at $v_{cont} \approx$ 0.21m/s for the case where $Q_{disp}$= 0.25ml/min, where there is a discontiuity in the drop diameter. The jetting velocity will also depend on the velocity of the dispersed phase. An increase of the dispersed phase will also make the detachent time shorter, because the critical size of the droplet will be reached faster. The critical jetting velocity is shown in Figure 3 for different

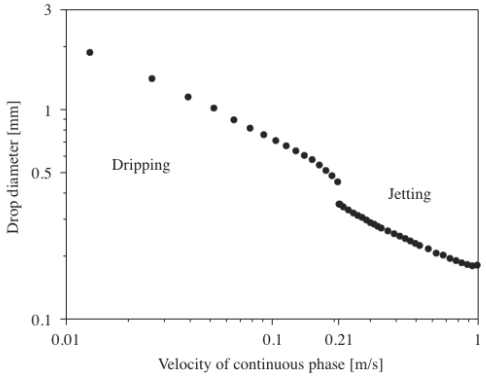


**Figure 2:** Drop diameter as a function of the velocity of the continuous phase. The rate of the dispersed phase is constant at $Q_{disp} = 0.25$ml/min. Figure adapted from [1].

dispersed phase velocities.

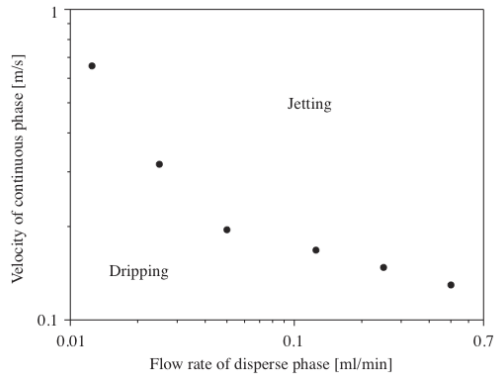


**Figure 3:** Critical jetting velocity as a function of the rate of the dispersed phase. Figure adapted from [1].

## 2.2 Continuous flow rate in the dripping mode

When the rate of the continuous phase ($v_{cont}$) is increasing the equilibrium between the interfacial tension and the hydrodynamic force is reached earlier and the time before the breakup of the droplet is shorter because of the rising drag force. Thus the drop size will decrease with the increase of $v_{cont}$,

since less disperse fluid is accumulated in the drop. The relation between the diameter of the drops and $v_{cont}$ was found experimentally by Cramer et al. [1] and is shown in Figure 4. At high velocities of the continuous phase

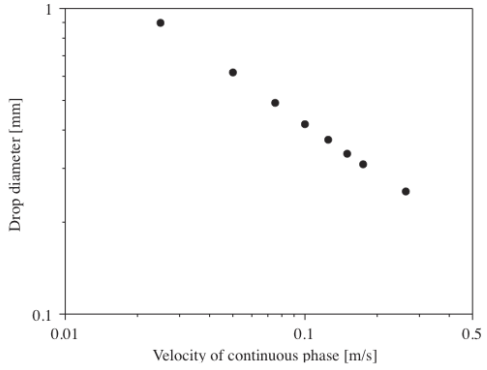


**Figure 4:** Drop diameter as a function of the velocity of the continuous phase. The rate of the dispersed phase is constant at $Q_{disp} = 0.025$ml/min. Figure adapted from [1].

more and larger satellite drops are generated. At high velocities there will be a longer thread between the drop and the capillary before the primary drop breaks, and due to the capillary pressure secondary drops are generated. This is shown in Figure 5. Also, the thread will accumulate more fluid volume, and the satellite drops become larger. Using a smaller channel for generation

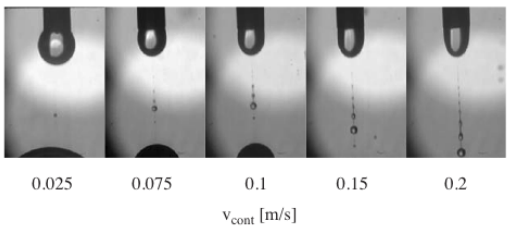


**Figure 5:** Generation of satellite drops through burst of the thread at different velocities of the contiuous phase. $Q_{disp} = 0.05$ml/min. Figure adapted from [1].

drops $< 100\mu$m Cramer et al. found the same behavior when changing the continuous phase velocity as for the droplets larger than $200\mu$m. The results

are shown in Figure 6. The drop diameter decreases with increasing flow rate of the continuous phase as for the larger droplets. The standard deviation is also included in the plot, and this was below 1% of the average value for most droplets.

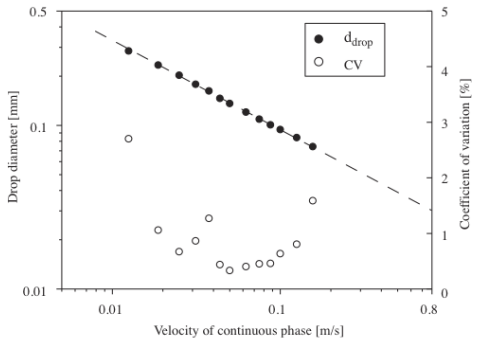


**Figure 6:** Droplet diameter as a function of velocity of the continuous phase in the small flow channel. $Q_{disp} = 6.25\mu$l/min. Figure adapted from [1].

## 2.3 Dispersed flow rate in the dripping and jetting mode

The phase of the dispersed fluid provides the fluid for the droplet formation and the rate will influence the size of the droplets. The effect of the velocity of the disperse phase was also studied by Cramer et al.[1]. Figure 7 shows an increase in the diameter as the flow rate of the disperse phase is increased. $Q_{disp}$ will determine the time until the equilibrium between the forces between the drop and flowing contiuous phase is reached. Higher flow rate will cause the critical size of the droplet to be reached faster, and the drop formation time will be smaller as shown in Figure 8. For high $Q_{disp}$ the necking and breakup prosses becomes dominant [6] [7], and the detachment point moves downstream in the channel. Therefore the velocity at the exit of the tube has little influence of the drop breakup and the necking process happens at the same time-scale for different disperse fow rates. Hence the drop formation time will be approximately constant at high flow rates of the dispersed phase and there will be a increase of the drop sizes.

Sharma et al.[5] observed the same effect in the jetting mode. As the velocity of the dispersed phase increases, the droplet diameter increases. Figure

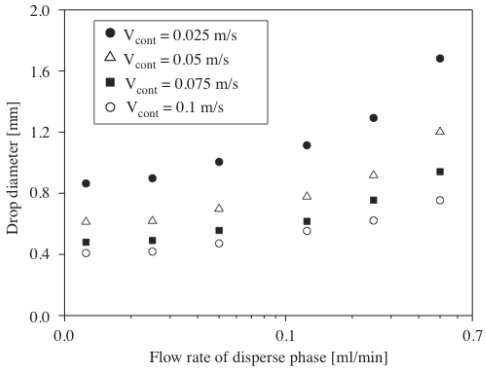


**Figure 7:** Drop diameter as a function of the dispersed flow rate at different velocities of the contiuous phase. Figure adapted from [1].

9 shows the diameter of droplets for three different dipersed flow rates.

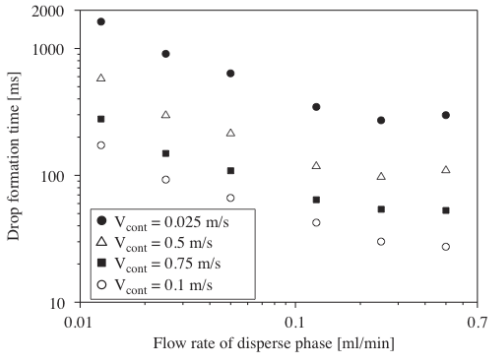


**Figure 8:** Drop formation time as a function of the disperse flow rate for different velocities of the continuous phase. Figure adapted from [1].

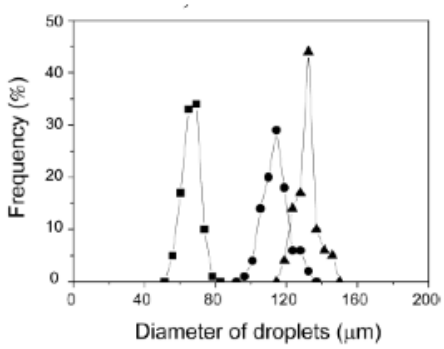


**Figure 9:** Size distribution of 2.0 wt% sodium-alginate extruded from a needle with 480$\mu$m inner diameter at () 1.2 cm/sec, (•) 2.6 cm/sec, and () 4.7 cm/sec into a co-flowing liquid paraffin stream with a flow rate of 17.5 cm/sec. Figure adapted from [5].

# 3 Effect of viscosities

The strength of the flow field involved in the drop formation is also affected by the viscosity of the fluids, as the momentum of the phases are increased. Cramer et. al. investigated the effect by increasing the viscosity of the dispersed phase while keeping the viscosity of the continuous phase constant. They observed that the dynamics of the necking and breakup was changed, with the viscous pressure opposing capillary pressure, creating longer threads. This provokes generation of a jet.

This has some implications on the droplet formation. First, the transition point between dripping and jetting is moved. Cramer et. al. found the critical jetting velocities for flows with different viscosity ratios $\lambda = \frac{\eta_{disp}}{\eta_{cont}}$. For $\lambda$<1, long threads between the capillary and droplet are formed in the dripping mode, and the transition point appears at low $v_{cont}$. For $\lambda$>1, the threads are only observed for high continuous phase velocities. The results are displayed in Figure 10.

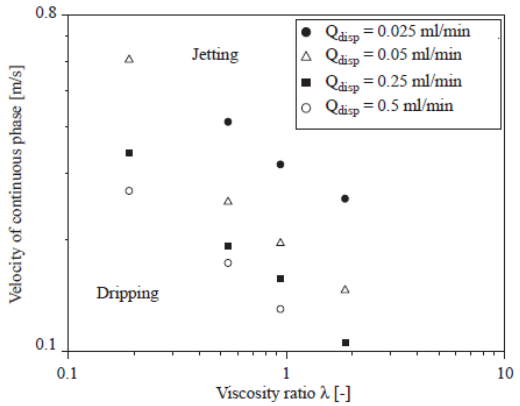


**Figure 10:** Critical jetting velocity at different flow rates as a function of viscosity ratios. Adapted from [1].

This tendency can also be seen in Figure 11. It also shows that in the dripping mode, which was what the authors focused on, the viscosity ratio has no apparent effect on the primary drop volume. However, after the primary drop has broken up, the increased viscous forces causes generation of satellite drops at the breaking up of the extended thread. The largest volume frac-

tion of satellite drops occur at high viscosity, $\eta_{disp} = 163$ mPas. In Figure

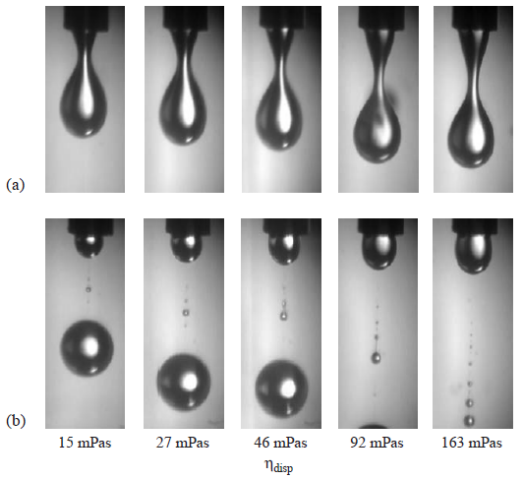


**Figure 11:** Drop formation at constant flow field at different viscosities. The velocity of the continuous phase is 0.15 m/s, while the flow rate of the dispersed phase is 0.025 ml/min. a) shows the stretching of the neck and the breaking up, while b) shows generation of satellite drops. Adapted from [1].

12 the drop diameter as a function of of disperse phase viscosity is shown for different velocities of the continuous phase and constant dispersed phase flow rate.

In the jetting mode, the viscosity will have a different effect. Sharma et. al. also did experimental studies on the effect of viscosity on the size of the droplets created in this regime. They used an aqueous polymer solution of mammalian cell-enclosing microcapsules dispersed in liquid paraffin. The results are shown in Figure 13, from which it can be concluded that increased viscosity makes the droplets made in the jetting regime smaller, but that this effect is less and less pronounced for higher continuous phase velocities. This is not explained by the authors.

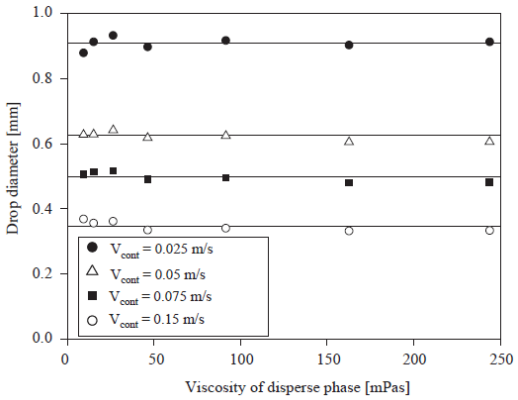


**Figure 12:** Droplet diameter as a function of viscosity ratio at different continuous phase velocities, with $Q_{disp} = 0.025$ ml/min. Adapted from [1].

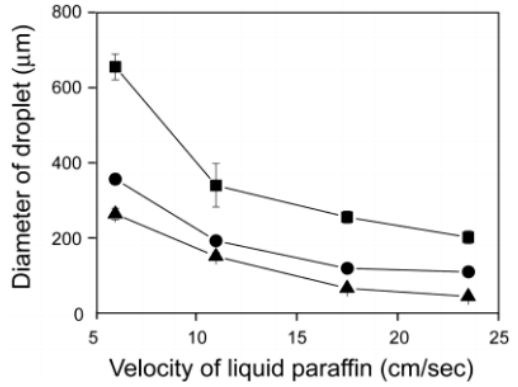


**Figure 13:** Droplet diameter as a function of continuous phase velocity for three aqueous solution viscosities: (square) 1.0, (dot) 36 and (triangle) 194 mPas. The velocity of the dispersed phase was 1.2 cm/sec and the size of the needle was 300 $\mu$m. The error bars represent standard deviation. Adapted from [5].

# 4 Interfacial tension and surfactant effects

Cramer et. al. also investigated the effect of interfacial tension on the drop formation. The fluids used to compare had similar densities, and the viscosity ratio between them was adjusted by the weight fraction of the additives. However, the interfacial tension in the two cases were different. The water/$\kappa$-Carrageenan 0.68 % system had higher interfacial tension than the water/PEG 12.5 % system, Figure 14 shows that the drop diameter was smaller in the latter case. The interfacial tension is the only force keeping

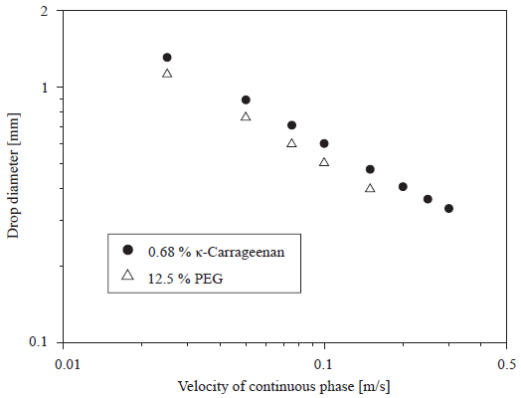


**Figure 14:** Droplet diameter as a function of continuous phase velocity for two different systems with the same viscosity ratio but different interfacial tension. $Q_{disp} = 0.05$ ml/min. Adapted from [1].

the droplet at the capillary tip, and reducing it means that the transition point is reached at an earlier point. On the other hand, the reduced the surfactants used to lower the interfacial tensions in such systems can have other effects too [4].

# 5 Conclusions

The experimental results referred to in the previous sections show a promising technique for generating monodisperse fluid droplet dispersions. The dripping mode should be used because a narrower size distribution is obtained, as well as the appearence of satellite drops are smaller. The formation rate is also very regular and uniform droplets are generated. The only force counteracting the drag in the continuous flow and momentum of the disperse phase, generating the fluid jet, is the interfacial tension. Increased continuous phase velocity and dispersed phase flow rate and viscosity provoke jet generation while lower interfacial tension decrease it. However, to be able to make small droplets, the continuous flow rates should be high. The effect of disperse flow rate on the size of the droplets is only present at relatively high rates, while the effect of viscosity is negligible in the dripping mode.

# References


[1] C. Cramer, P. Fischer, E. J. Windhab. *Drop formation in a co-flowing ambient fluid.* Ch. Eng. Sci. 59, pp 3045-3058, 2004.

[2] P. B. Umbanhowar, V. Prasad, D. A. Weitz. *Monodisperse emulsion generation via drop break off in a coflowing stream.* Langmuir 16, pp 347-351, 2000.

[3] C. Clanet, J. Lasheras. *Transition from dropping to jetting.* Journal of Fluid Mechanics 383, pp 307-326, 1999.

[4] Y. Cui, N. R. Gupta. *Surfactant effects on drop formation in co-flowing fluid streams.* Colloids and Surfaces A: Physicochem. Eng. Aspects 393, pp 111121, 2011.

[5] A. Sharma, R. Sharma *Mammalian cells in nanocapsules:fiber production in co-flowing ambient liquid stream.* Nanotech 3, pp 282-285, 2010.

[6] D. Zhang, H. Stone. *Drop formation in viscous flows at a vertical capillary tube.* Physics of fluids 9, 2234-2242, 1997

[7] X. Zhang *Dynamics of drop formation in viscous flows.* Chemical Engineering Science 54, 1759-1774, 1999

# List of Figures

# Bibliography


[1] K. B. Kjerstad, *Clay-Oil Droplet Suspensions in Electric Field*, Master's Thesis, NTNU, (2012)

[2] A. Mikkelsen *Experimental Studies of Flow- and Electric Properties of Oil Droplets Including Suspended Clay Particles*, Master's Thesis, NTNU, (2012)

[3] P. Dommersnes, Z. Rozynek, A. Mikkelsen, R. Castberg, K. Kjerstad, K. Hersvik and J. O. Fossum. Active structuring of colloidal armour on liquid drops. *Nat. Commun*, **4**, 2066, (2013).

[4] D. J. Griffiths, *Introduction to electrodynamics.* Third edition, Person Education, (2008)

[5] C. T. O'Konski, H. C. Thatcher, The distortion of aerosol droplets by an electric field. *J. Phys. Chem.*, **57**, 955-958 (1953).

[6] R. S. Allan and S. G. Mason, Particle Behaviour in Shear and Electric Fields. I. Deformation and Burst of Fluid Drops. *Proc. R. Soc. Lond. A* **267**, (1962)

[7] G. Taylor, Studies in electrohydrodynamics. I. The circulation produced in a drop by electrical field. *Proc. R. Soc. Lond. A.* **291**, 159-166 (1966).

[8] F. Salipante and P. M. Vlahovska, Electrohydrodynamics of drops in strong uniform dc electric fields. *Phys. Fluids* **22**, 1-9 (2010).

[9] D.A. Saville, Electrohydrodynamics: The Taylor-Melcher Leaky Dielectric Model. *Annu. Rev. Fluid Mech.* **29**, 27-64, (1997).

[10] G. Quincke, Ueber Rotationen im constanten electrischen Felde. *Ann. Phys. Chem.* **59**, 417-468 (1896).

[11] Z. Rozynek, K. D. Knudsen, J. O. Fossum, Y. Mheust, B. Wang and M. Zhou, Electric field induced structuring in clay-oil suspensions: new insights from WAXS, SEM, leak current, dielectric permittivity, and rheometry. *J. Phys.: Condens. Matter* **22** 324104, (2010).

[12] J. C. Baygents, N. J. Rivette and H. A. Stone, Electrohydrodynamic deformation and interaction of drop pairs. *J. Fluid Mech.* **368**, 359-375 (1998).

[13] C. N. Baroud, F. Gallaire and R. Dangla, Dynamics of microfluidic droplets. *Lab Chip* **10**, 2032-2045 (2010).

[14] C. Cramer, P. Fischer, E. J. Windhab. Drop formation in a co-flowing ambient fluid. *Ch. Eng. Sci.* **59**, 3045-3058 (2004).

[15] O. Vizika and D. A. Saville, The electrohydrodynamic deformation of drops suspended in liquids in steady and oscillatory electric fields. *J. Fluid Mech.*, **239**, 1-21, (1992).

[16] H. Hemmen, *Experimental Studies of Smectite Clays: Colloids and Nanoporous Materials.* PhD Thesis, NTNU (2012).

[17] F. Bergaya, B. K. G. Theng and G. Lagaly, *Handbook of Clay Science.* Elsevier Ltd. (2006).

[18] B. Ruzicka and E. Zaccarelli, A fresh look at the Laponite phase diagram. *Soft Matter*, **7**, 1268-1286 (2011)

[19] J. O. Fossum, Y. Méheust, K. P. S. Parmar, K. D. Knudsen, K. J. Måløy and D. M. Fonseca, Intercalation-enhanced electric polarization and chain formation of nano-layered particles. *Europhysics Letters* **74**, 438-444, (2006).

[20] K. P. S. Parmar, Y. Mheust, B. Schjelderupsenand and J. O. Fossum, Electrorheological Suspensions of Laponite in Oil: Rheometry Studies. *Langmuir* **24**, 1814-1822, (2008).

[21] V. Rives *Layered Double Hydroxides: Present and Future.* Nova Science Publishers: New York, (2001).

[22] X.Q. Hou, D.L. Bish, S.L. Wang, C.T. Johnston, R.J. Kirkpatrick, Hydration, expansion, structure, and dynamics of layered double hydroxides. *Am. Mineral.* **88**, 167-179, (2003).

[23] T. Kameda, S. Saito, Y. Umetsu, Mg-Al layered double hydroxide intercalated with ethylene-diaminetetraacetate anion: Synthesis and application to the uptake of heavy metal ions from an aqueous solution. *Sep. Purif. Technol.*, **47**, 20-26, (2005).

[24] G.R. Williams and D. O'Hare, Towards understanding, control and application of layered double hydroxide chemistry. *J. Mater. Chem.* **16**, 3065-3074, (2006).

[25] J.-H. Choy, S.-J. Choi, J.-M. Oh and T. Park, Clay minerals and layered double hydroxides for novel biological applications. *Appl. Clay Sci.* **36**, 122-132, (2006).

[26] N. P. Ashby and B. P. Binks. Pickering emulsions stabilised by Laponite clay particles. *Chem. Phys.* **2**, 5640-5646, (2000).

[27] Y. Nonomura and N. Kobayashi. Phase inversion of the Pickering emulsions stabilized by plate-shaped clay particles. *J. Colloid Interface Sci.* **330**, 463-466, (2009).

[28] A. D. Dinsmore, M. F. Hsu, M. G. Nikolaides, M. Marquez, A. R. Bausch and D. A. Weitz, Colloidosomes: Selectively Permeable Capsules Composed of Colloidal Particles. *Science* **298**, 1006-1009, (2002).

[29] R. Parthibarajan, C. R. Reichel, N. L. Gowrishankar and D. Pranitha, Colloidosomes drug delivery - A review. *Int. J. Pharm. Biol. Sci.* **1**, 183-197, (2011).

[30] S. Jiang, Q. Chen, M. Tripathy, E. Luijten, K. S. Schweizer and S. Granick, Janus particle synthesis and assembly. *Adv. Mater.* **22**, 1060, (2010).

[31] C. Kaewsaneha, P. Tangboriboonrat, D. Polpanich, M. Eissa and A. Elaissari, Janus colloidal particles: preparation, properties, and biomedical applications. *ACS Appl. Mater. Interfaces* **5**, 1857, (2013).

[32] A. Synytska, R. Khanum, L. Ionov, C. Cherif, C. Bellmann. Water-repellent textile via decorating fibers with amphiphilic Janus particles. *ACS Appl. Mater. Interfaces* **3**, 1216, (2011).

[33] M. Lattuadaa and T. A. Hattonb, Synthesis, properties and applications of Janus nanoparticles. *Nano Today* **6**, 286, (2011).

[34] A. B. Subramaniam, M. Abkarian, H. A. Stone, Controlled assembly of jammed colloidal shells on fluid droplets. *Nat. Mater.* **4**, 553, (2005).